United States Geological Survey Earthquake Hazards Program
Final Technical Report

Award #: G18AP00082

Title: Investigating unrecognized earthquake faults in the Carson Domain, Walker Lane

Author:
Andrew V. Zuza
Nevada Bureau of Mines and Geology
Mackay School of Earth Sciences and Engineering
University of Nevada, Reno
1664 N. Virginia St
Reno, NV 89557

Phone: (775) 784-1446
Fax: (775) 784-1709
Email: azuza@unr.edu

Other personnel:
Michael C. Say, University of Nevada, Reno, Masters Student

Term: 09/01/2018-08/31/2019

Abstract

The northern Walker Lane, stretching from ~40 km north of Reno, NV to Carson City in the south, accommodates ~5-7 mm/yr of northwest-trending right-lateral shear, and a poorly constrained portion of this motion is occurring along orthogonal northeast-striking left-slip faults. The Carson Domain of the northern Walker Lane consists of three northeast-striking faults. Based on a regional analysis of fault spacing and the seismogenic zone thickness across the entire Walker Lane, two additional northeast-striking left-slip faults were predicted to exist in the Carson Domain between already documented faults. In this study, we conducted detailed geologic mapping (1:24,000 scale) in the northern Pine Nut Mountains to (1) investigate whether there is a previously unrecognized left-slip fault in this location, and (2) constrain the age of recent strike-slip and normal faulting in the map area for seismic hazard considerations. The northern Pine Nut Mountains consist of a Jurassic metavolcaniclastic unit (i.e. the Gardnerville Formation), Oligocene ash-flow tuff, and Miocene-Pliocene intermediate-felsic volcanic rocks. New U-Pb zircon geochronology confirms an Early Jurassic age for the Gardnerville Formation and new $^{40}Ar/^{39}Ar$ geochronology yielded 7.30-7.15 Ma ages for the Miocene volcanic rocks. Our new mapping identified mostly east-dipping dip-slip normal faults that crosscut the Miocene volcanic rocks, and we interpret they were active after the youngest dated volcanic rock was deposited (i.e., after 7.15 Ma). Observed geometries and fault offsets suggest that the northern Pine Nut Mountains accommodated 0.5 mm/yr west-east extension since this time, in agreement with present-day rates from geodesy and other more regional-based estimates. This study also suggests that westward Basin and Range encroachment on the Sierra Nevada block occurred after 7.15 Ma. We found evidence for a poorly exposed northeast-striking fault in the Bull Canyon drainage, based primarily on unit discordance across the drainage, which we term the Bull Canyon fault. We suggest that this fault was a left-slip fault because (1) it merges to the southwest with a major north-striking dip-slip down-east normal fault, (2) where exposed exhibited subhorizontal striations, and (3) parallels a minor left-slip fault that offsets volcanic units. The fault is not active, and is covered by Qao and younger deposits. Accordingly, we interpret that the Bull Canyon left-slip fault was active sometime in late Cenozoic (Miocene-Pliocene), possibly displacing units 1-2 km left laterally based on kinematically linked normal-fault-based offsets. In this sense, the Bull Canyon fault may have been parallel and similar to other Carson Domain faults, but has since become inactive. Our study also confirmed the presence of north-striking uphill-facing Quaternary fault scarps along the western part of the study area that displace Qfo fan surfaces but are covered by intermediate-young Quaternary fan surfaces. The Quaternary Fault and Fold Database currently lists these as left-slip, but our field observations suggest they are either dip-slip normal or oblique right-slip normal.

Introduction

The combined Walker Lane (WL) and Eastern California Shear Zone (ECSZ) make up a broad northwest-trending intracontinental right-lateral shear zone that accommodates 15-25% (Dixon et al., 2000; Thatcher, 2003; Hammond and Thatcher, 2007; Hammond et al., 2011) of the ~50 mm/yr Pacific-North American relative plate motion (DeMets and Dixon, 1999; Thatcher et al., 2016) (Fig. 1). However, observed fault geometries and slip histories across the

Walker Lane reveal a complex interaction between strike-slip faults with varying kinematics and off-fault deformation (Wesnousky et al., 2005a, 2005b; Faulds and Henry, 2008) (Figs. 1 and 2). There are numerous domains of parallel strike-slip faults, and many oblique to the regional shear zone trend (Fig. 1). Decades of research has focused on trying to understand how shear strain is accommodated across the WL-ECSZ (e.g., Slemmons et al., 1979; Stewart 1980; Stewart 1988; Dixon et al., 1995; Cashman and Fontaine, 2000; Oldow et al., 2001; Surpless et al., 2002; Unruh et al., 2003; Wesnousky, 2005a, 2005b; Henry and Faulds, 2007; Wesnousky et al., 2012; Bormann et al., 2016; Li et al., 2017; Sturmer and Faulds, 2018).

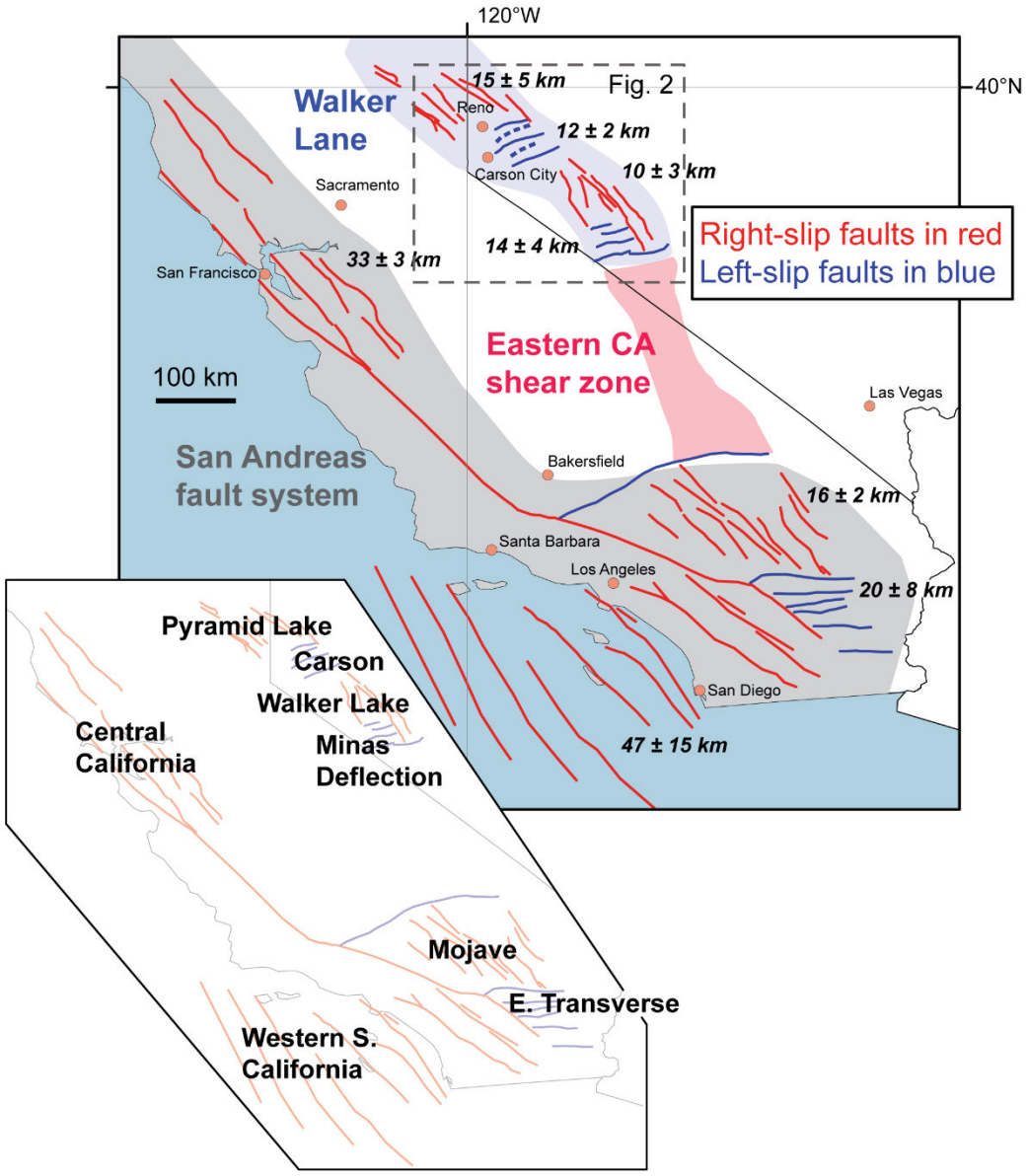

Figure 1. Parallel strike-slip fault domains (Stewart, 1988; Faulds and Henry, 2008) in the San Andreas and Walker Lane fault systems (Faulds and Henry, 2008; Wesnousky et al., 2012). Numbers correspond to average fault spacing data from Zuza et al. (2017) and Zuza and Carlson (2018). Inset shows the names of each strike-slip fault domain, and dashed blue lines near Carson City represent hypothesized left-slip faults. Also shown is the location of Figure 2.

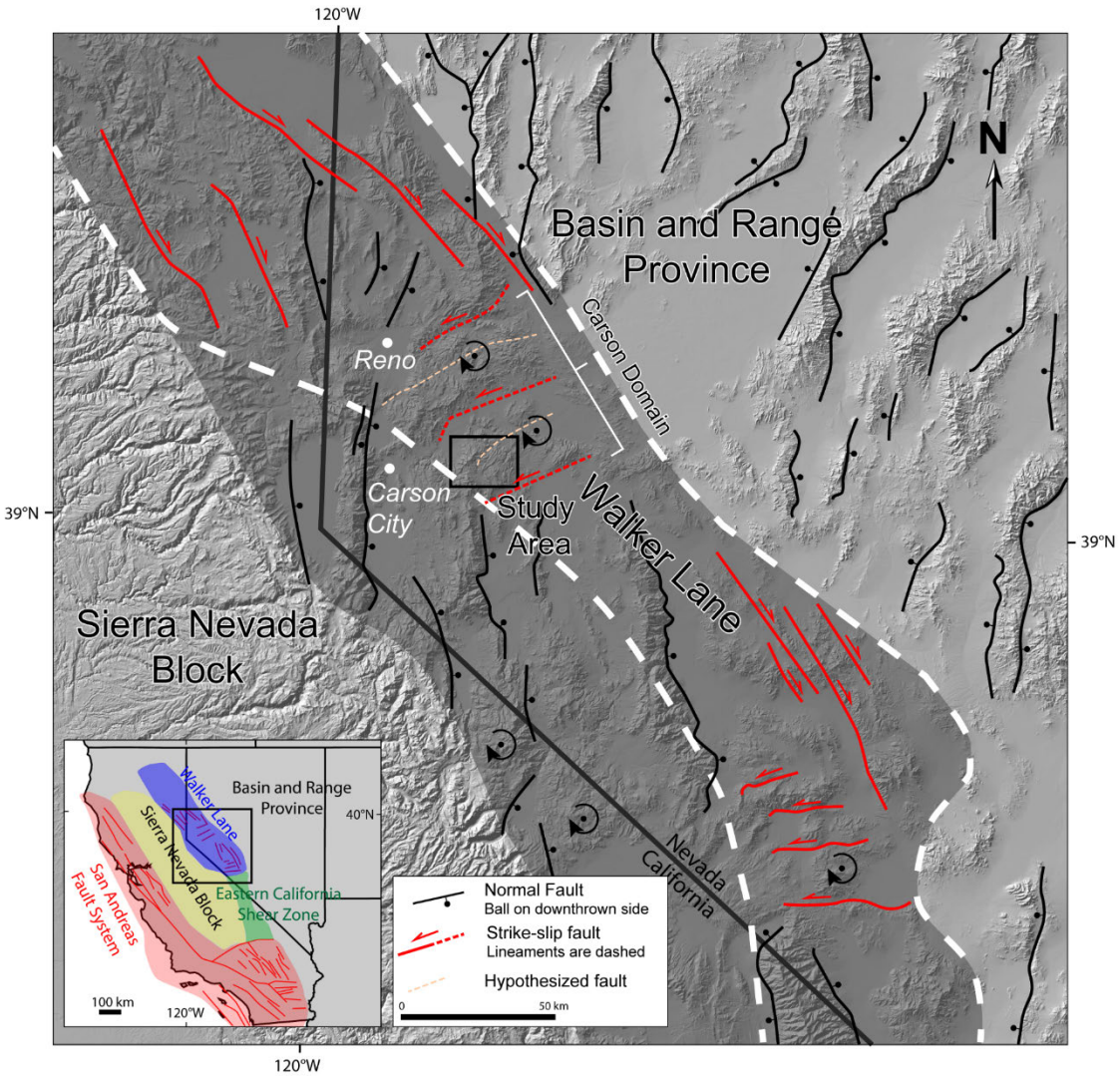

Figure 2. Sketch map of the northern and central Walker Lane showing the study area of the northern Pine Nut Mountains within the Carson Domain. Gray Walker Lane outline is the boundary of Wesnousky (2005) and white dashed outline is the boundary of Faulds and Henry (2008).

In the northern Walker Lane, which encompasses the distributed shear zone from ~40 km north of Reno, NV to Carson City, NV in the south (Fig. 2), geodetic data recognizes 5-7 mm/yr of northwest-trending right-lateral shear (Bennet et al., 2003; Hammond and Thatcher, 2007). The Carson Domain (Figs. 1 and 2) is particularly enigmatic. It consists of three east-northeast-striking faults that have been related to clockwise rotation of the fault-bounded crust, leading to estimated slip rates on these structures of 0.7-1.6 mm/yr (Cashman and Fontaine, 2000; Wesnousky et al., 2012; Li et al., 2017) (Fig. 2). The combination of relatively slow slip rates and lack of vertical offset on individual faults (i.e., predominately strike-slip offset) has made recognition and evaluation of all of these faults challenging (e.g., Wesnousky et al., 2005a, 2005b; 2012), which is problematic from both shear-strain tabulation and seismic hazard perspectives.

The Carson Domain traditionally consists of three northeast-striking structures (Fig. 2), but regional analysis of fault spacing and the seismogenic zone thickness across the entire Walker Lane (Zuza et al., 2017; Zuza and Carlson, 2018), discussed briefly below, predicts that there may be two additional, previously unrecognized strike-slip faults in the Carson Domain. This prediction was corroborated by preliminary remote sensing and existing geologic maps (Stewart, 1999). For this project, we tested the hypothesis that the Carson Domain of the northern Walker Lane is comprised of five northeast striking left-slip faults, as opposed to the currently recognized three strike-slip faults (Fig. 2). This work involved detailed field mapping around the location of one of the inferred strike-slip faults, in the northern Pine Nut Mountains, with the intent of documenting a through-going strike-slip fault and deciphering the timing of most recent activity. The study area consisted of Miocene-to-present volcanic rocks that were ideal for documenting the age of structures because crosscutting relationships could be dated.

The work summarized in this report documented a probable left-slip fault in the northern Pine Nut Mountains that crosscuts volcanic rocks that are 7.15 Ma and other younger, but undated, volcanic rocks. Additional geochronology on the youngest displaced rocks is in progress. Based on the orientation and inferred displacement of the fault, which we refer to as the Bull Canyon fault based on its occurrence in the Bull Canyon drainage, it appears that this fault was comparable to the other Carson Domain left-slip faults. Therefore, our novel methodology of using readily observable fault spacing versus seismogenic zone thickness relationships to identify previously unrecognized faults was successful. However, our field observations suggest that the strike-slip fault is not an active structure, and thus its seismic hazard is negligible. We also documented north-striking normal faults along the western flank of the northern Pine Nut Mountains that displace old Quaternary alluvial surfaces (middle to early Pleistocene?).

Rationale

It has been documented that for continental strike-slip fault systems with multiple domains of parallel evenly-spaced strike-slip faults, the spacing of strike-slip faults is often linearly related to the thickness of the seismogenic crust, which may approximate the brittle crust (Zuza et al., 2017; Zuza and Carlson, 2018; Yang et al., 2019). This is similar to the long-recognized observation that joint spacing in sedimentary-rock outcrops is linearly proportional to the thickness of each joint hosting sedimentary bed (e.g., Lachenbruch, 1961; Hobbs, 1967; Narr and Suppe, 1991; Gross et al., 1995). A noteworthy benefit of analyzing fault-spacing (S) vs seismogenic zone thickness (L) is that both variables are readily available in the western U.S.: strike-slip fault spacing may be obtained from published maps (e.g., Stewart, 1999; Faulds and Henry, 2008; Wesnousky et al., 2012) (Fig. 1) and high-resolution relocated earthquake-location data is available in the San Andreas and Walker Lane regions (Schaff and Waldhauser, 2005; Lin et al., 2007; Waldhauser and Schaff, 2008; Hauksson et al., 2012).

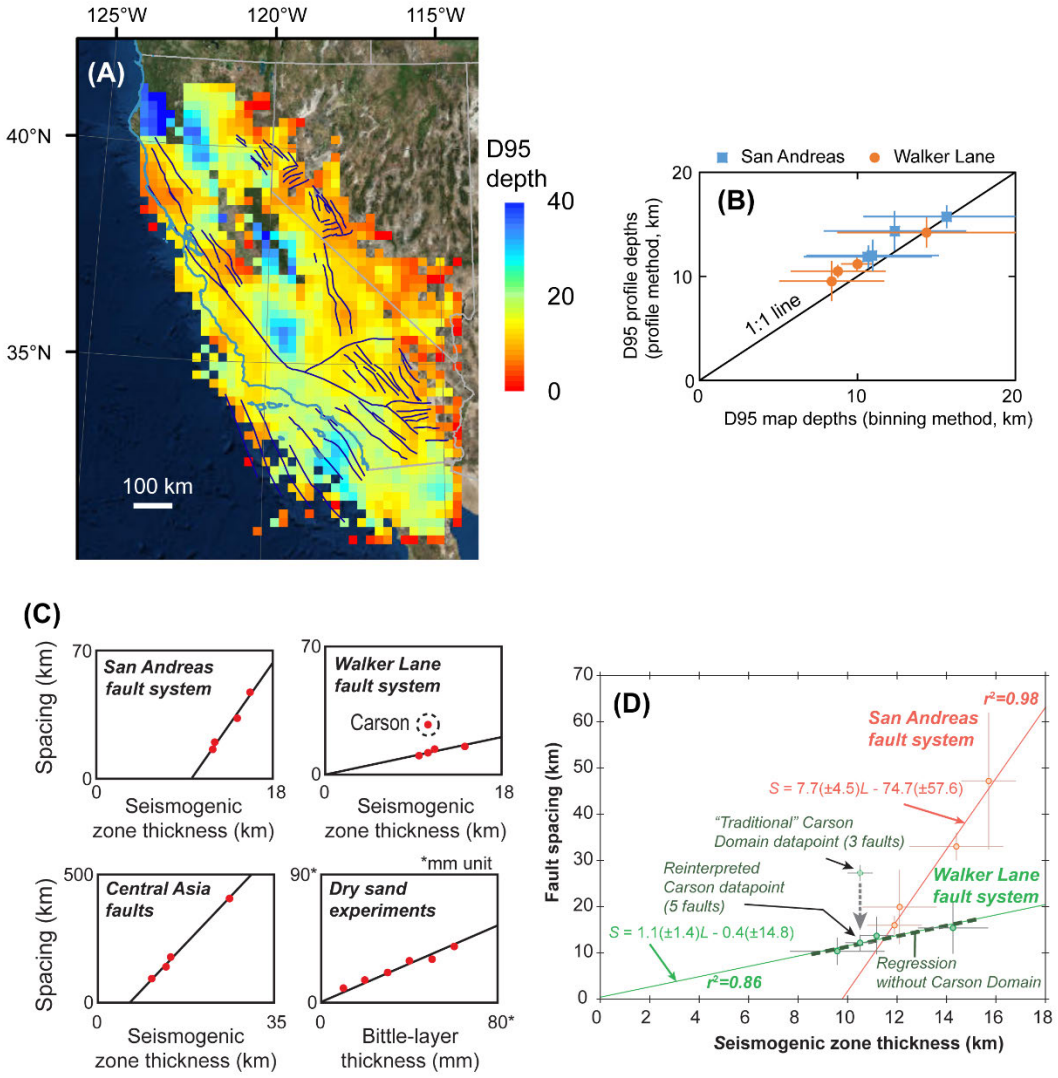

Figure 3. (A) D95 map (22.5-km bin width) for the California filtered with a Gaussian lowpass filter. (B) Comparison of seismogenic thickness depths (D95 depths) estimated by projecting earthquakes onto vertical profiles (e.g., Zuza et al., 2017; Zuza and Carlson, 2018) versus earthquake binning as presented in Fig. 3A. Note that most data falls along a 1:1 line. (C) Fault spacing vs seismogenic zone thickness for the San Andreas, Walker Lane, Central Asia, and modeled analog strike-slip fault systems showing that all data can be fit by a linear regression, with the exception of the original three-fault Carson Domain datapoint (Zuza et al., 2017; Zuza and Carlson, 2018). (D) Seismogenic zone thickness versus fault spacing for the San Andreas (red) and Walker Lane (green) fault systems. Note that the Carson Domain data point is not in line with the other three Walker Lane points; these three other data points (i.e., Pyramid Lake region, the Minas Deflection, and the Walker Lake region) can be fit with a linear regression (thick green dashed line). Reinterpretation of the Carson Domain with five strike-slip faults moves this datapoint in line with the other three. Thin lines represent best-fit linear regressions of the modified Walker Lane data and the San Andreas data.

Here we extracted seismogenic zone thickness via two methods, both constraining the cutoff depths above which 95% (D95) of the observed seismicity occurs is calculated (e.g., Sibson, 1982; Chiarabba and De Gori, 2016): (1) by projecting earthquake events onto a vertical plane perpendicular to the strike of a given fault system and calculating D95 along the length of

the profile (Zuza and Carlson, 2018), and (2) by binning the earthquake data into fixed width bins (e.g., 22.5 km wide bins) and calculating the D95 depth of each bin (Zuza and Cao, in review) (Fig. 3A). Both methods yielded similar seismogenic thickness results for the various domains (Fig. 1) within the Walker Lane (Fig. 3B).

In general, fault spacing plotted against seismogenic zone thickness results in a clear linear relationship (see the San Andreas and Central Asia data in Fig. 3C). The same trend is observed for scaled analogue experiments using frictional materials (Zuza et al., 2017) (Fig. 3C). Most of Walker Lane data also follows a linear *S* vs. *L* relationship, with the exception of the Carson Domain data (Fig. 3D). Data from three of the fault domains (i.e., Northern Walker Lane, North of Minas, and the Minas Deflection) (Fig. 1), excluding the Carson results, shows a clear linear relationship (thick green dashed line in Fig. 3D). The original three-strike-slip-fault Carson data (i.e., spacing of 27±3 km) plots significantly off this line (Fig. 3D). However, evidence from remote sensing and existing geological maps (Stewart, 1999) suggest the presence of two additional major strike-slip faults (Zuza and Carlson, 2018). If correct, this addition would reduce fault spacing *S*, and a reinterpreted five-fault fault spacing (i.e., spacing of 12±2 km) vs seismogenic zone thickness for the Carson Domain plots in line with the Walker Lane data (Fig. 3D) (Zuza and Carlson, 2018). This deviation from a linear *L* vs *S* relationships for strike-slip faults is the only one we are aware of for continental strike-slip faults, in sandbox models, and for Saturn's Moon Enceladus (Yin et al., 2016; Zuza et al., 2017; Zuza and Carlson, 2018; Yang et al, 2019), and thus this project sought to investigate whether there are previously unrecognized strike-slip faults in the Carson Domain that may affect this relationship.

Geologic setting

The Pine Nut Mountains are located in a complex structural setting within the western Basin and Range dip-slip extensional province and the Walker Lane right-slip transtensional shear zone (Fig. 2) (Surpless et al., 2002; Faulds and Henry, 2008; Cashman et al., 2009). Specifically, they are the westernmost structural and topographic expression of the Basin and Range extensional province and are also located within the Carson Domain of the northern Walker Lane (Dilles and Gans, 1995; Henry and Perkins, 2001; Surpless et al., 2002; Li et al., 2017). The Carson Domain traditionally consists of three parallel northeast-striking left-slip faults that are oriented orthogonal to the northwest trend of the Walker Lane (Fig. 1). Right-lateral shear across this domain is accommodated via clockwise vertical-axis rotation of semi-rigid fault-bounded blocks, which results in estimated ≤1 mm/yr slip rates on left-slip faults (Cashman and Fontaine, 2000; Li et al., 2017; Sturmer and Faulds, 2018).

The Pine Nut Mountains consists of Jurassic Gardnerville Formation (Noble, 1962; Schweickert, 1978; Stewart, 1997) and Jurassic-Cretaceous granodiorite to granite (e.g., Dilles and Wright, 1988), which are unconformably overlain by Oligocene ash-flow tuff and Miocene-Pliocene volcanic rocks (e.g., Fultz et al., 1984; Vikre and McKee, 1994; Henry et al., 2012) (Fig. 4). Mesozoic granitic intrusions are not exposed in the study area in the northern Pine Nut Mountains, but they do comprise much of the range to the south (e.g., Surpless et al., 2002; Cashman et al., 2009). Thermal modeling of apatite fission track (AFT) data from granites to the south suggest that exhumation of the Pine Nut Mountains and tilting of the range initiated

sometime after ca. 10-5 Ma (Surpless et al., 2002). Geologic mapping of Miocene sediments by Cashman et al. (2009) suggested that normal faulting in the Carson Range initiated after ca. 7 Ma. To better bracket the timing of fault activity via cross-cutting relationships, we conduced detailed characterization and dating of the Miocene-Pliocene volcanic rocks, which is discussed in the next section.

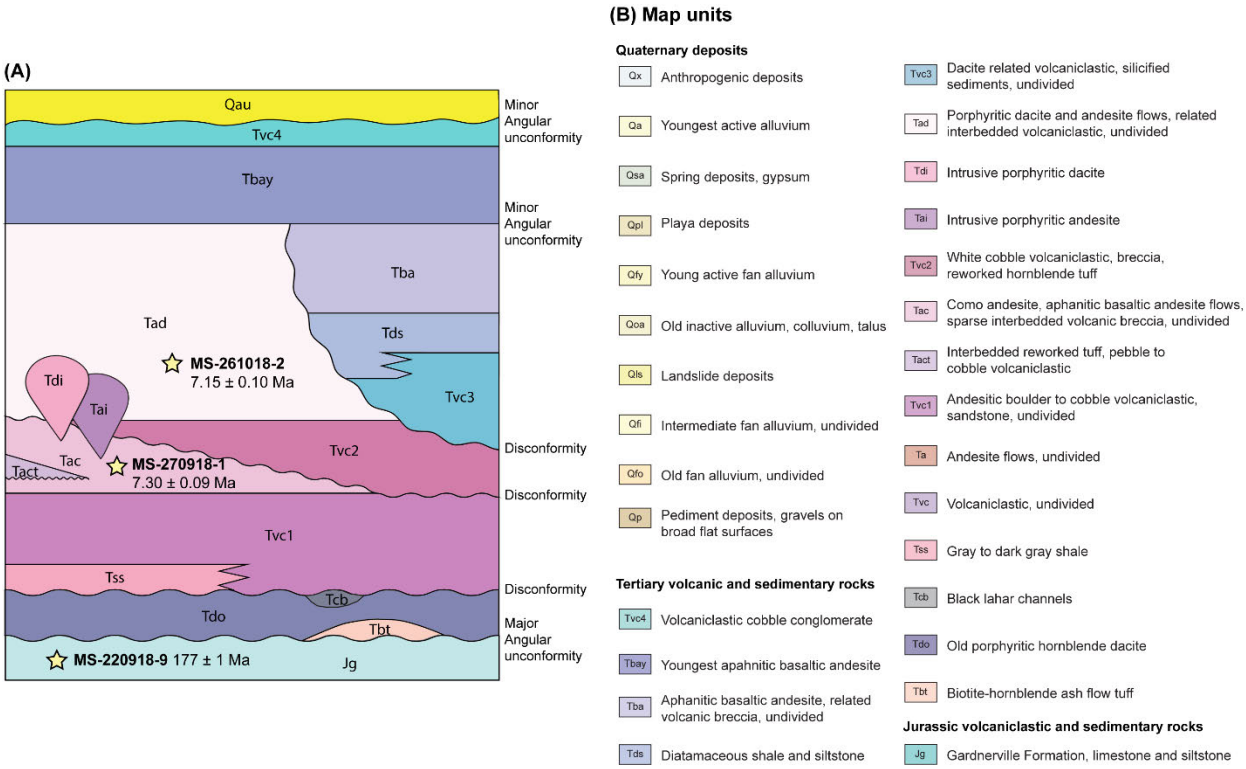

Figure 4. (A) Schematic stratigraphic column of the map units in the study area showing relative stratigraphic relationships. New geochronology ages from this study shown with stars. (B) Map units for new geologic map in Figure 5.

Methods

The PI and a graduate student conducted 1:24,000-scale geologic mapping along one of these inferred strike-slip faults in the northern Pine Nut Mountains, just east of Carson City (Fig. 2). The full-scale map is provided in the appendix and Figure 5 is a scaled version of this map. Mapping built upon previous geologic maps, including the 1:100,000 scale Carson City quadrangle (Stewart, 1999) and smaller maps of the Como mining district located within the study area (Russell, 1981; Vikre and McKee, 1994). New geologic mapping was focused along the northeast-trending Bull Canyon river valley, which was interpreted to have a strike-slip fault, and the main range to the west that was cut by north-striking east-dipping normal faults (Fig. 5A). A cross section was constructed across the map area to convey the structural style and estimate the magnitude of late Cenozoic extension (Fig. 5B).

To better define the map units, including the age of volcanic rocks that were displaced by mapped faults, we systematically documented the late Cenozoic volcanostratigraphy (Fig. 4). This included Miocene-Pliocene basaltic andesite to dacite. Existing published ages from within

the study area consist of K/Ar ages from volcanic rocks within the Como Mining District (Fig. 4). The ages range from 7-6 Ma for andesite flows and 5-3 Ma for the overlying dacitic volcanic rocks (Vikre and McKee, 1994). To characterize these volcanic rocks, we conducted additional thin-section petrography, whole-rock geochemistry, and $^{40}Ar/^{39}Ar$ geochronology. In particular, the age of the units that are crosscut by faults provides timing constraints for faulting. Cenozoic volcanic rocks were unconformably deposited on a Mesozoic metavolcaniclastic unit—the Jurassic Gardnerville Formation—and we conducted zircon U-Pb geochronology to confirm the unit's age.

Geochemistry

Most of the units in the map area consist of basaltic andesite to dacite volcanic flows. We conducted whole-rock geochemical analyses of the representative units, and 37 samples were collected, cleaned, and crushed for analyses. We used 10-50 grams of sample per analysis, which were done by ALS Geochemistry in Reno, Nevada. Major elements analyses were completed by fused bead and acid digestion preparation and analyzed using an inductively coupled plasma atomic emission spectroscopy (ICP-AES). Rare and trace element analysis were also completed by fused bead and acid digestion preparation and analyzed using an inductively coupled plasma mass spectrometer (ICP-MS). For classification and discrimination diagrams, major oxides were normalized to 100%, excluding loss on ignition (LOI).

Geochronology

New $^{40}Ar/^{39}Ar$ hornblende geochronology was performed on the volcanic strata in the northern Pine Nut Mountains. Thin-section observations guided sample selection, and hornblende grains were separated from unaltered representative samples. Samples were irradiated at the USGS TRIGA reactor in Denver, CO, and analyses were completed at the New Mexico Tech Geochronology Research Laboratory using procedures described in McIntosh et al. (2003) and Henry et al. (2017). Given the high effective closure temperature of Ar in hornblende (i.e., 500—550°C), depending on cooling rate and grain properties (Harrison, 1982; McDougall and Harrison, 1999), we interpret that $^{40}Ar/^{39}Ar$ ages reflect the eruption age of the dated volcanic rock.

Zircon U-Pb geochronology was conducted on a volcanic breccia from the Jurassic Gardnerville Formation to verify the age of this unit. Zircon grains were separated via standard crushing, sieving, magnetic, and heavy liquid methods. Grains were mounted in 1" epoxy rounds, polished, and imaged on a scanning electron microscope (SEM) with a cathodoluminescence (CL) detector to reveal internal grain structure to guide analyses and interpretations. Zircons were analyzed via laser ablation inductively coupled plasma mass spectrometer (LA-ICP-MS) at the University of Nevada, Reno. Standards included low uranium 91500 (1062 Ma; Wiedenbeck et al., 2004), high uranium Plesovice (337 Ma; Sláma et al., 2008), and TEMORA 1 (416 Ma; Black et al., 2003). Data was reduced and plotted using Isoplot v. 4.1 (Ludwing, 2012). Analyses more than 90% normally discordant and 5% reversely discordant were not considered in our final age calculation.

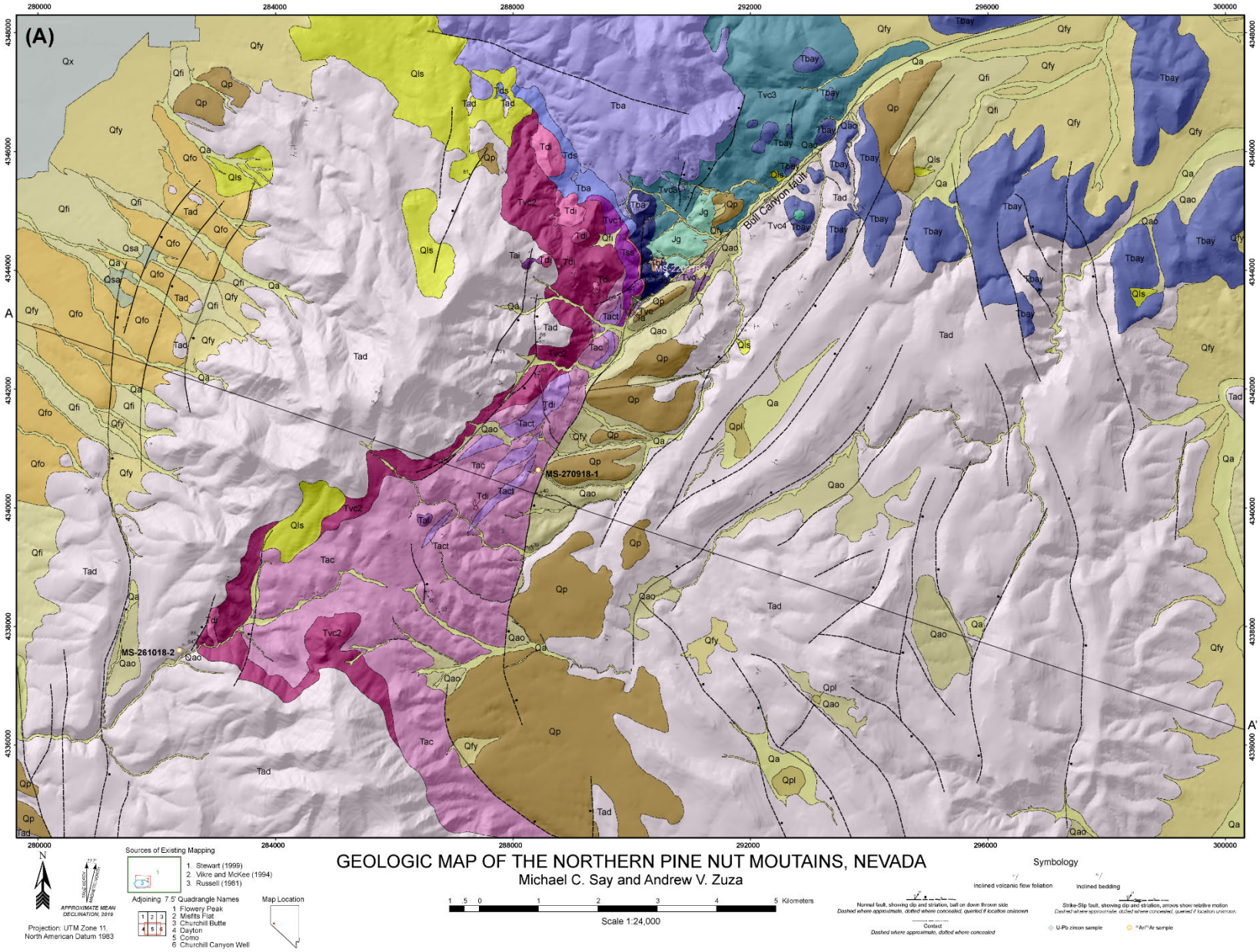
(A)
A
A'
Bull Canyon fault
MS-270918-1
MS-261018-2
280000
284000
288000
292000
296000
300000
4348000
4346000
4344000
4342000
4340000
4338000
4336000
Sources of Existing Mapping
1. Stewart (1999)
2. Vikre and McKee (1994)
3. Russell (1981)
Adjoining 7.5' Quadrangle Names
1 Flowery Peak
2 Misfits Flat
3 Churchill Butte
4 Dayton
5 Como
6 Churchill Canyon Well
Map Location
N
APPROXIMATE MEAN DECLINATION, 2019
Projection: UTM Zone 11, North American Datum 1983
GEOLOGIC MAP OF THE NORTHERN PINE NUT MOUTAINS, NEVADA
Michael C. Say and Andrew V. Zuza
1 .5 0 1 2 3 4 5 Kilometers
Scale 1:24,000
Symbology
Inclined volcanic flow foliation
Inclined bedding
Normal fault, showing dip and striation, ball on down thrown side
Dashed where approximate, dotted where concealed, queried if location unknown
Strike-Slip fault, showing dip and striation, arrows show relative motion
Dashed where approximate, dotted where concealed, queried if location unknown
Contact
Dashed where approximate, dotted where concealed
U-Pb zircon sample
40Ar/39Ar sample

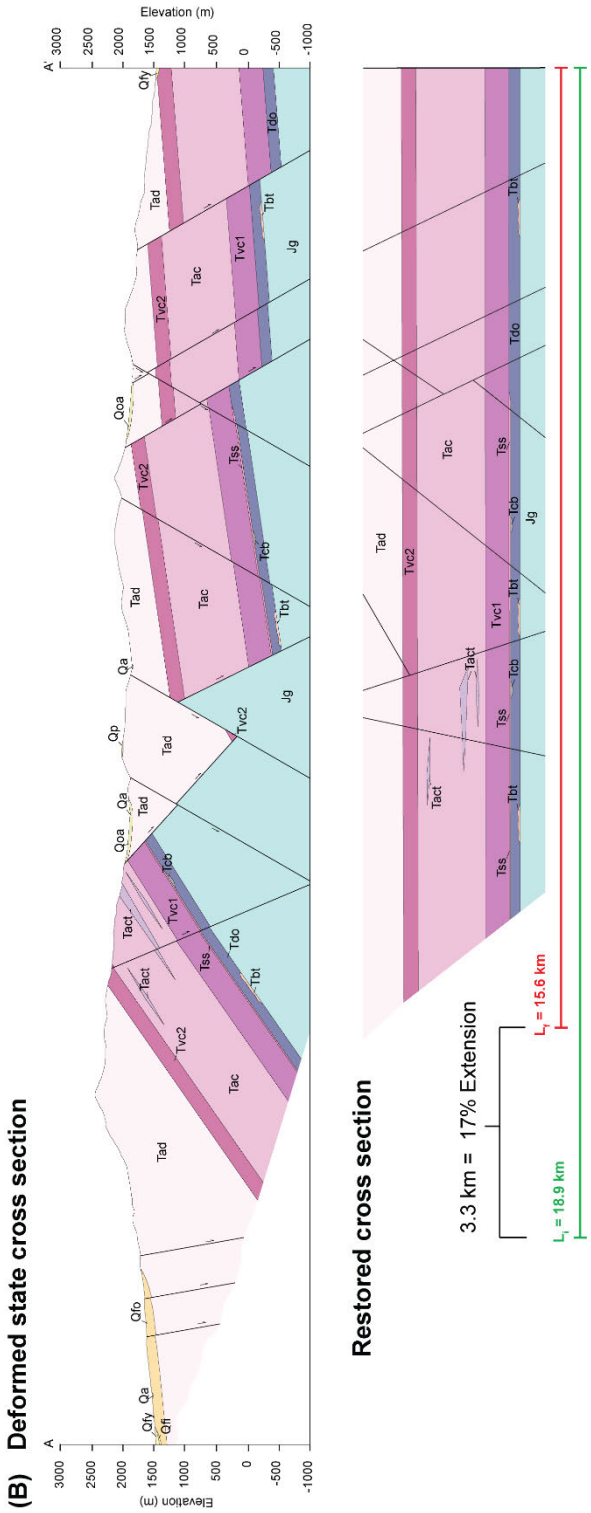

Figure 5. (A) Simplified geologic map of the study area. The map was constructed at 1:24,000 scale but its size was reduced for this report. Geochronology samples are shown. The full-scale map is provided in the Appendix. (B) Cross section across the study area and line-length restoration assuming only dip-slip normal faulting. Note that the scale of the geologic map cross section may not the same in this report.

Analytical Results

Geochemistry

Complete geochemical data is shown in Appendix Table 1 and sample locations are marked on the full-scale appendix map. Most samples are intermediate to felsic (~55-65% SiO_2) calc-alkaline volcanic rocks (Fig. 6). Samples are predominately metaluminous (all are $Al_2O_3/(Na_2O+K_2O) > 1$ and most are $Al_2O_3/(CaO+Na_2O+K_2O) < 1$). Rare earth element (REE) patterns are fairly steep, and samples were enriched in Ba and Sr, depleted in Nb and Ti, and appear geochemically indistinguishable from similar-aged Ancestral Cascades volcanic rocks found around Lake Tahoe and Reno, NV (Fig. 6C) (Cousens et al., 2008).

Geochronology

Two samples were dated via $^{40}Ar/^{39}Ar$ geochronology: MS-261018-2, a dacite (unit Tad) that was stratigraphically higher than Como andesite sample MS-270918-1 (unit Tac). Vikre and McKee (1994) dated samples from Tad and Tac, and obtained whole-rock K/Ar ages of 4.6 ± 0.2 Ma to 2.8 ± 0.1 Ma for Tad and 7.5 ± 0.3 Ma to 6.0 ± 0.7 Ma for Tac. Complete $^{40}Ar/^{39}Ar$ information for our new analyses are in Appendix Table 2 and spectra are displayed in Figure 7. Sample MS-261018-2 (unit Tad) yielded a plateau age of 7.15 ± 0.10 Ma (Fig. 7A) and sample MS 270918-1 (unit Tac) yielded a plateau age of 7.30 ± 0.09 Ma (Figs. 7B). Although the ages overlap within uncertainties, the stratigraphically higher sample MS-261018-2 did yield a younger age than sample MS-270918-1, as expected (Fig. 4 A). Our new Tac age of ca. 7.30 Ma overlaps the K/Ar ages of Vikre and McKee (1994) for this unit, but our Tad age of ca. 7.15 Ma is dissimilar to the Vikre and McKee (1994)'s K/Ar ages for this unit. The younger Tad ages obtained by Vikre and McKee (1994) may reflect problems with the K/Ar methods relative to $^{40}Ar/^{39}Ar$ dating, complications from whole-rock dating versus single phase analyses, or younger alteration or reheating of the Tad unit.

Zircon grains from Gardnerville Formation sample MS-220918-9 were analyzed to constrain the age of this unit. Complete isotopic information is in Appendix Table 3. Analysis of 160 zircon grains from Gardnerville Formation sample MS-220918-9 yielded ages spanning ca. 153 Ma to ca. 198 Ma, although many were >10% normally discordant (Fig. 7C). Ages broadly define a normal distribution around 175-180 Ma, and the weighted mean age of 89 concordant analyses was 177 ± 1 Ma (MSWD: 2.4) (Fig. 7C). Zircons from the Gardnerville Formation volcanic breccia sample reflect Early-Middle Jurassic volcanism proximal to the study area. We conservatively assign an Early Jurassic age of ca. 177 Ma to this Gardnerville Formation sample. However, the weighted mean age of youngest concordant zircon grains could also be used to define a maximum depositional age; the three youngest grains yielded an age of 168 ± 3 Ma (MSWD: 0.4) (Fig. 7C).

Map area stratigraphy

Mesozoic Basement and Oligocene Ash-Flow Tuffs

The oldest rocks in the northern Pine Nut Mountains are metasedimentary and metavolcanic rocks of the Jurassic Gardnerville Formation (unit Jg; Noble, 1962; Stewart, 1997)

(Fig. 4). Our ca. 177 Ma U-Pb zircon ages presented above confirms this age assignment. The unit is comprised of thinly bedded shale, with the best outcrops located along incised channels. There are sparse outcrops of massive intensely veined gray limestone. The total thickness of the formation is not exposed in the study area. It is likely more than several kilometers thick but poorly constrained (Noble, 1962). The Gardnerville Formation is assumed to underlie Cenozoic volcanic rocks across the study area.

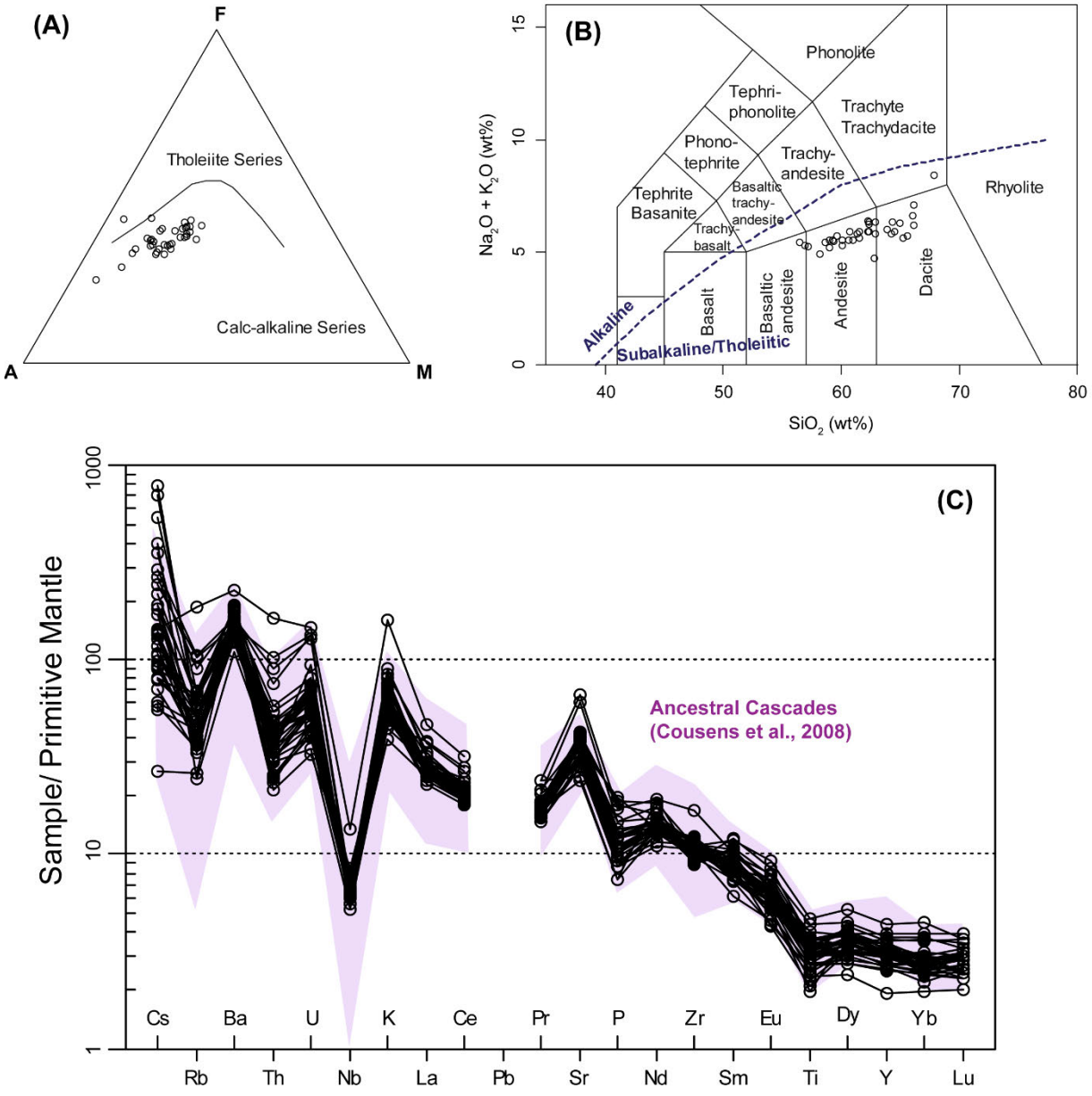

Figure 6. Geochemical data from the Miocene-Pliocene volcanic rocks from the northern Pine Nut Mountains. (A) AFM (Na_2O+K_2O–FeO–MgO ternary) with tholeiite versus calc-alkaline divisions of Irvine and Baragar (1971). (B) Total alkalis versus silica (TAS) diagram of Le Bas et al. (1986). (C) Primitive mangle normalized (Sun and McDonough, 1989) trace element patterns for samples from the northern Pine Nut Mountains and published data from other volcanic rocks around Lake Tahoe and Reno, NV, that have been interpreted as part of the Ancestral Cascades (purple) (Cousens et al., 2008).

The Oligocene ash-flow tuff (unit Tbt) was deposited over Mesozoic basement rocks as an angular unconformity. Tbt is exposed as a small outcrop in the northern portion of the map are with a thickness of 15 m. The tuff is moderately welded and composed of quartz, sanidine, and euhedral biotite. The tuff is dacitic (68% SiO_2) and consists of lapilli pumice fragments with angular lithic clasts of andesite up to 1 cm in diameter. Other similar Oligocene ash-flow tuffs are observed to the east and west of the study area, deposited unconformably on Mesozoic basement (i.e., Mickey Pass tuff, Nine Hill tuff, and Singatse tuff; Stewart, 1999).

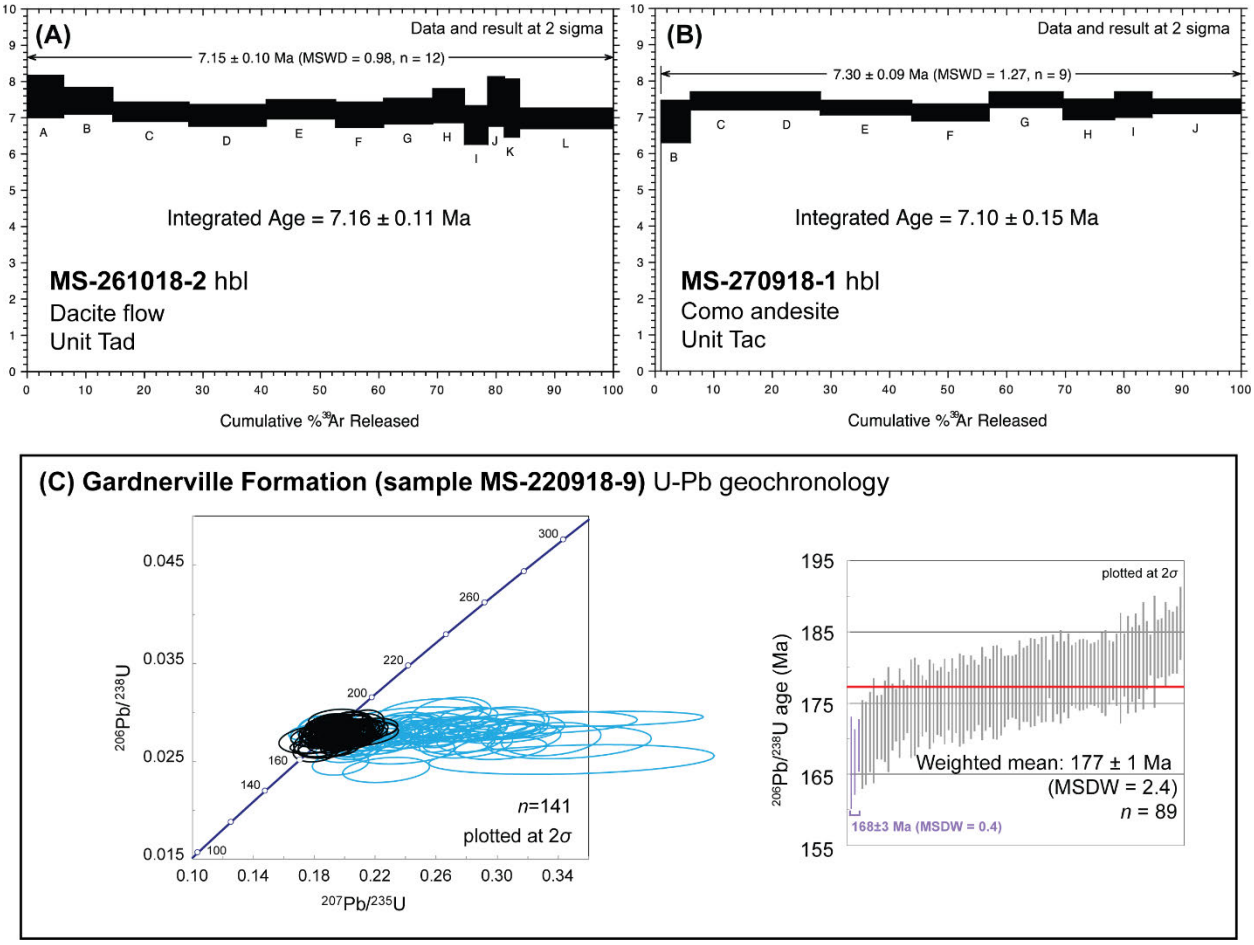

Figure 7. Geochronology from this study, including (A-B) $^{40}Ar/^{39}Ar$ geochronology on hornblende grains (hbl) from two volcanic units (i.e., Tad and Tac) and (C) zircon U-Pb geochronology on a volcanic breccia from the Gardnerville Formation.

Miocene-Pliocnee Volcanic Flows and Related Sedimentary Rocks

A gray hornblende dacite (unit Tdo) (64-66% SiO_2) overlies the Tbt and Mesozoic basement rocks (Fig. 4). The dacite is 60-70 m thick and the unit is composed of hornblende, plagioclase, biotite, and sparse quartz. Hornblende grains are up to 0.5 cm and are highly chloritized. The upper contact of the dacite contains discontinuous incised channels of massive silt-supported black lahar and conglomerate deposits (unit Tcb) up to 10 m thick. The hornblende dacite is capped by a 15 m thick gray colored shale (unit Tss), which is overlain by volcaniclastic debris flows (unit Tvc1) composed of subangular to subrounded boulder to cobble clasts of

andesite in a sandy-ash matrix (Fig. 4). The lower portion of the unit contains channels of massive tan colored sandstone and pyroclastic flows exhibiting angular clasts of dull green tuff (5 cm). A thin flow of aphanitic black to dark gray andesite is poorly exposed in the lower portion of Tvc1.

Late Miocene Como Andesite

The Como andesite (unit Tac) consists of andesite flows (58-61% SiO_2) interbedded with reworked tuff, pyroclastic flow deposits (unit Tact), and shallow intrusions (Fig. 4). The lower contact of the Como andesite is not exposed but the unit may be >1 km thick as determined by cross-section geometries (Fig. 5B). The lower portion of the Como andesite is comprised of aphanitic andesite flows interbedded with discontinuous pale blue, green, and gray colored massive reworked tuff and pyroclastic flows that contain matrix supported, rounded andesite pebble to cobble clasts up to 30 cm. The aphanitic andesite is composed of hornblende, plagioclase, clinopyroxene, and orthopyroxene. The lowest exposed portion of the Como andesite yielded a hornblende $^{40}Ar/^{39}Ar$ age of 7.30 ± 0.10 Ma (Fig. 7B). The upper portion of the Como andesite is mostly poryphyritic andesite to basaltic andesite with some aphanitic flows composed of plagioclase, clinopyroxene, orthopyroxene, and hornblende laths up to 5 mm. The reworked tuff and pyroclastic flows contain rounded to subangular clasts of andesite and tuff ranging in size from 1 m to centimeter size clasts. The interbedded reworked tuff is highly altered to montmorillonite, quartz, chlorite, and pyrite throughout Tac (Vikre and McKee, 1994). The reworked tuff outcrops in pale green to pale purple in color with alteration obscuring much of the original bedding and flow foliation. Alteration is confined these interbedded units and the contact with adjacent andesite due to the high permeability of the clast rich reworked tuff and pyroclastic flows.

Dacite and Andesite Flows

The dacite unit with minor interbedded andesite flows (unit Tad) is the most widespread unit in the study area. Tad is exposed in topographically high regions in the west and occupies the majority of the study area to the east. The unit is >1.5 km thick, but the upper contact is not exposed in the study area. The basal section is composed of volcaniclastic, hornblende-bearing pyroclastic, and debris flows (unit Tvc1) that vary in thickness along strike. The overlying porphyritic dacite flows (62-65% SiO_2) are composed of plagioclase, hornblende, biotite, and quartz. The age of the lower portion of the dacite flows is 7.15 ± 0.10 Ma (Fig. 7A). Sparse thin flows of aphanitic andesite and volcanic debris flows are interbedded in portions of the dacite. Shallow sills and dikes (units Tdi and Tai) (Fig. 4) intruded the volcaniclastic debris flows and dacite flows in the western map area (Fig, 5).

Late Miocene to Younger Basaltic Andesite

The youngest volcanic rocks are exposed in the northern map area, and although the contacts are poorly exposed, they appear to unconformably overlie Tad and Tvc2. The oldest of these younger flows consists of volcaniclastic debris flows, tuff beds, and tuffaceous sedimentary rocks (unit Tvc3) (Fig. 4). The sedimentary sequence has been pervasively silicified, hindering identification of the protolith. Diatomaceous shale and sandstone (unit Tds) overlie Tvc3 and

outcrop as white float with little-to-no bedding exposures. Aphanitic basaltic andesite flows (unit Tba) (56-59% SiO_2) overlie the sedimentary packages in the north and are composed of glassy groundmass, plagioclase, and clinopyroxene. The youngest aphanitic basaltic andesite (unit Tbay) in the map area is exposed in the northeast part of the study area and lies as an angular unconformity over the dacite flows. The young basaltic andesite outcrops as foliated volcanic flows and in one location a volcaniclastic debris flows (unit Tvc4) conformably cap the unit. The aphanitic basaltic andesite flows consist of plagioclase, clinopyroxene, orthopyroxene, and glassy groundmass.

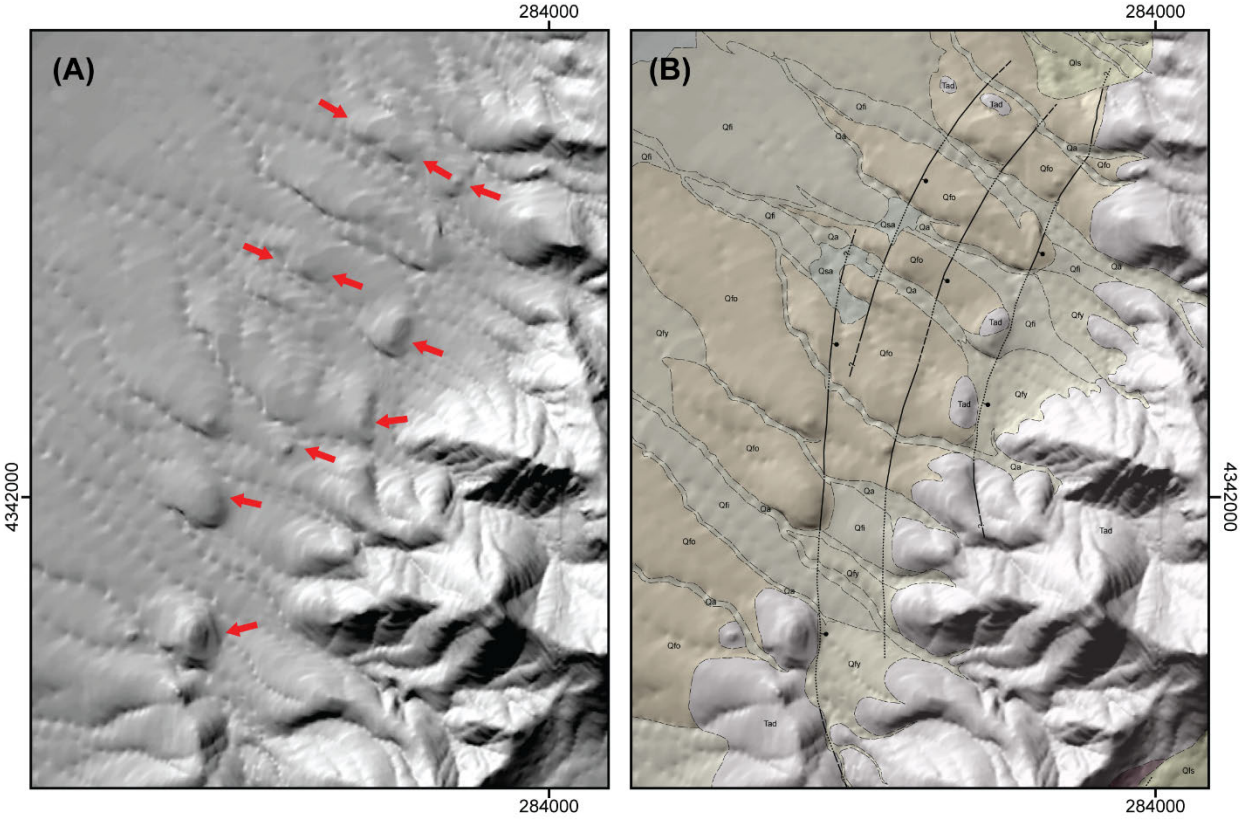

Figure 8. (A) 10 meter (1/3 arc second) resolution elevation hillshade from the northwestern edge of the map area. Elevation data shows distinct lineaments connecting uphill-facing scarps that cut Quaternary fans (scarps are marked with red arrows). (B) Geologic map overlay of elevation hillshade image shows faults cut old fan alluvium (Qfo) and bedrock. Largest scarp heights are ~20 m high. Note that this figure is at a difference scale from the geologic maps.

Quaternary Deposits

A series of alluvial fans, basin fill, landslide deposits, playa deposits, and alluvial pediments of varying Quaternary ages occur adjacent to the eastern and western flanks of the range and in fault-bounded basins throughout the study area (Fig. 5A). The alluvial fans in the map area display varying degrees of surface composition and morphology that we grouped into three relative age units: Qfo, Qfi, and Qfy (Fig. 5). The fault bounded basins in the central and eastern portion of the area of study contain basin fill and active playa deposits formed by seasonal lakes. The majority of the pediment deposits occur along the eastern range front fault

(Fig. 3). These deposits exhibit broad flat surfaces of moderate to poorly sorted gravels to occasional boulders and are deeply incised (~100 meters) by active channels.

Structural Framework

Multiple fault strands were observed across the northern Pine Nut Mountains (Fig. 5A). Figure 9 summarizes the major fault structures and attitudes observed in this study area. Most faults strike north (334-029º) and dip east, with observed striations trending east to northeast (Fig. 9B). Most striations suggest dip-slip displacement, although several suggest oblique left-lateral normal-sense displacement. A minor set of faults strike northeast-east (030-084º) with shallow striation plunges suggesting some lateral offset (Fig. 9B).

The largest fault in the study area is a north-striking east-dipping normal fault that defines the eastern flank of the main Pine Nut range (Fig. 9A). The fault has a curvilinear trace that strikes north in the south map area and gradually bends to strike northeast to the north. Striation measurements along the southern strand suggest dip-slip motion (average striation trend/plunge: 070°/40°), whereas the northern fault strand has more shallowly plunging striations (average striation trend/plunge: 030°/10°). Because the fault trace is fairly continuous, we interpret that the fault transitions from north-striking dip-slip normal-sense motion to northeast-striking oblique left-lateral normal motion along the Bull Canyon drainage. There are no fault exposures in the Bull Canyon drainage, but the juxtaposition of different volcanic units requires some concealed fault within the main drainage. We interpret that this drainage covers a left-slip fault that we herein refer to as the Bull Canyon fault. Other evidence for this fault includes Jg basement placed against Tad with geometries that are inconsistent with simple normal faulting and rotation (Fig. 5A). Furthermore, a small outcrop of Tvc is juxtaposed against Jg, near sample MS-220918-9 (Fig. 5A), which can be explained by oblique left-lateral normal fault motion on the Bull Canyon fault. Parallel to the Bull Canyon fault, we documented a small vertical left-slip fault that offsets Tvc2 through Tdo units (Fig. 5A). We are unable to determine if the fault cuts the youngest basaltic andesite unit (Tbay) (Fig. 5A) in the northeast because the fault trace is concealed by active alluvium. The fault has not been recently active and it is covered by Qao/Qfo and younger deposits (Fig. 5A).

The dominant east-dipping normal faults in the range resulted in westward tilting of the Miocene volcanic rocks 30-36° (Fig. 9D). If this tilting started after the youngest age from Tad in the main part of the range (i.e., 7.15 Ma), this equates to westward tilting rates of 4.2-5°/myr. The younger, but currently undated volcanic rocks in the northern part of the study area (i.e., Tvc3, Tds, Tba, Tbay, and Tvc4) (Fig. 5A), are 18-24° shallower than those observed in the main part of the range (Fig. 9E). The simplest interpretation is that the younger volcanic rocks were deposited sometime after extension and range tilting had started, and are thus synkinematic volcanic rocks indicative of tilt fanning.

Fault scarps cut Quaternary fans on the western flank of the range (Fig. 8). Uphill-facing scarps (east-dipping) offset older alluvial fans (Qfo) that contain pediments of bedrock (Fig. 8). The scarp heights vary but are roughly 20 meters high in some places. The east-dipping faults strike north and bend towards a north-northeast strike at their northern extent in the map area.

Several springs and spring deposits are found along the fault traces. Further south along the western active fault trace, a small depression of fill alluvium and older alluvium is present adjacent to the east side of the fault (Fig. 8). Young, active, and intermediate aged alluvial fan deposits (Qa, Qfy, and Qfi) cover the fault traces and indicate the age of faulting was pre-deposition of these units.

Discussion

The primary goal of this study was to investigate the presence of an active northeast-striking left-slip fault in the northern Pine Nut Mountains. Our detailed geologic mapping suggests that this fault exists in the Bull Canyon river drainage (Fig. 5A). The fault is not active and does not displace Qao and younger deposits. Although exposures of the fault are scarce, we documented several locations with northeast-striking fault exposures with shallowly plunging fault striations. We made no direct observation of the kinematics of this fault, but unit geometries and a parallel left-slip fault are consistent with the fault having some left-lateral component. We also note that the Bull Canyon fault merges with the major north-striking east-dipping normal fault that defines the eastern flank of the range in the study area (Fig. 5A). If these structures were kinematically linked, east-dipping normal-sense motion (toward 070°) suggests left-slip kinematics on the Bull Canyon fault. Our cross section across the major east-dipping normal fault suggests 3.5-4 km of east-directed normal-sense displacement (Fig. 5B). We acknowledge that more conservative drafting of the cross section could minimize displacement to ~3 km based on geometries of the hanging wall. Considering the geometries of these respective fault systems, a speculative conservative range of 3-4 km normal-sense offset on the eastern range-bounding fault suggests that the Bull Canyon left-slip fault may have accommodated up to 1.7-2.3 km of displacement (Fig. 9C).

Line-length restoration of our cross section suggests that the northern Pine Nut Mountains accommodated 3.3 km of west-east extension (17% extensional strain) (Fig. 5B). A regional compilation of extension across the Great Basin based on published geologic maps suggested 4.1 km across the Pine Nut Mountains (20% extensional strain) (Long, 2018). We find that the general agreement with our calculations compared to a regional estimate bolster our estimates. Tad was the youngest unit that is displaced within our cross section, and our age for this unit of ca. 7.15 Ma can be used to calculate a minimum extensional rate of 0.5 mm/yr over geologic timescales. This equates to an extensional strain rate of 7.5×10^{-16} s^{-1}. Geodetic extensional strain rates across this region are on the order of 9×10^{-16} s^{-1} to 3×10^{-15} s^{-1} (Kreemer et al., 2012). If these faults initiated more recently, the rates would be higher. Similarly, we can calculate slip rates on the Bull Canyon left-slip fault of 0.2-0.3 mm/yr. This rate is comparable, but slightly slower, than estimates on the Olinghouse fault to the north (Fig. 2) (0.3-0.6 mm/yr geologic slip rates from Sturmer and Faulds, 2018; <1 mm/yr Quaternary slip rates from Li et al., 2017). However, because the Bull Canyon left-slip fault is not active today, it may have moved at faster rates before becoming an inactive structure. Alternatively, some component of the dip-slip normal faulting may not transfer to left-slip faulting, either due to variable strain partitioning or a temporal switch in kinematics, which would reduce estimates of offset and slip rates.

The Miocene package of volcanic rocks observed in the main range of the study area are conformable and parallel, which implies that they were not deforming during deposition. The observed structures and our new ages suggest that late Cenozoic deformation did not occur in this region until after 7.15 Ma. This implies that normal faulting initiated after 7.15 Ma as Basin and Range extension affected the northern Pine Nut Mountains. This initiation age is compatible with other estimates, including Cashman et al. (2009), whom suggested that normal faulting in the Carson Range initiated after ca. 7 Ma, and AFT modeling by Surpless et al. (2002) that suggested normal faulting and range tilting initiated sometime after 10-5 Ma.

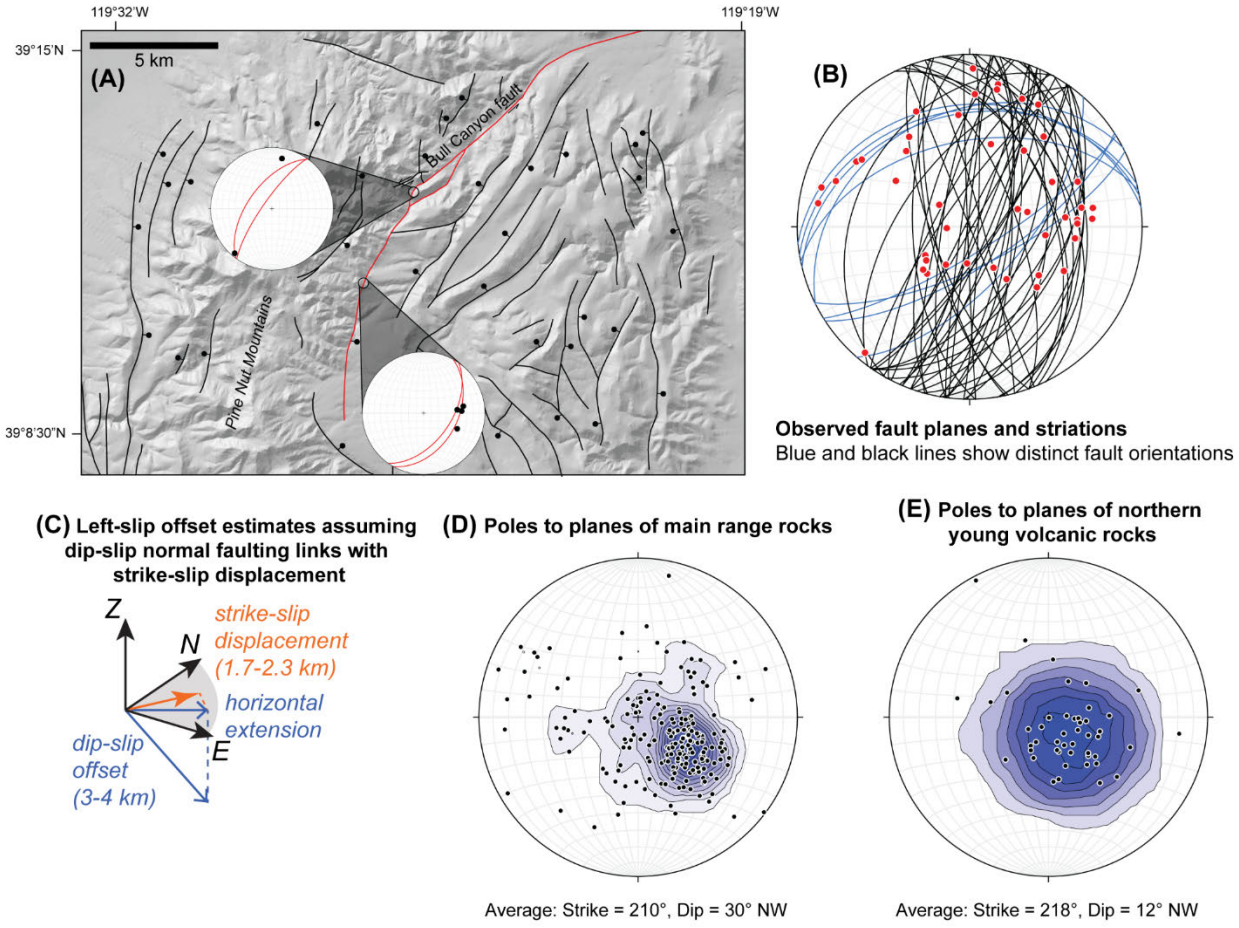

Figure 9. (A) Sketch fault map for the study area, with the interpreted left-slip Bull Canyon fault and its linkage with a north-striking normal fault highlighted in red. Two stereonets show fault attitudes and striations at two locations of this fault. (B) Stereonet showing fault orientations and striations (red circles) across the study area. Note that most faults are north-striking with a smaller population of northeast-east-striking faults. (C) Geometric and kinematic relationships between dip-slip normal faulting on the major north-striking east-dipping normal fault (blue arrows) and left-slip displacement on the Bull Canyon fault (orange arrow). Black arrows are coordinate axes north (N), east (E), and up (Z). (D-E) Poles to planes of (D) volcanic strata observed in the main Pine Nut Mountains range and (E) younger volcanic rocks in the northern part of the study area. Note that the older volcanic rocks dip 18° steeper than the relatively younger volcanic rocks.

There is discordance between the Miocene volcanic rocks in the main range and the younger volcanic rocks along the northern part of the map area (Figs. 9D and E), which we

interpret as tilt fanning. There is no age for these younger volcanic rocks, but we infer that they were deposited after tilting of the main range had initiated, leading to discordance of 18-24°. An age of these units would allow for better constrained tilt versus time histories. However, we can make some speculative calculations. Assuming a constant tilting rate of 4.2-5°/myr since 7.15 Ma, we predict the ages of these younger volcanic rocks to be in the 3-4 Ma age range. We note that although Vikre and McKee (1994)'s K/Ar ages spanning 4-3 Ma are inconsistent with our new $^{40}Ar/^{39}Ar$ ages, their data does suggest some thermal pulse and cooling during this interval, potentially related to the deposition of these younger undated basaltic units.

Along the western flank of the range in the western map area, we observed north-striking faults that cut Quaternary fan surfaces (Fig. 8). The U.S. Geological Survey Quaternary Fault database (https://earthquake.usgs.gov/hazards/qfaults/) lists some of these faults as latest Quaternary (<15 ka) with left-slip kinematics. Our only constraints on the age of these faults are that they cut Qfo fans but not Qfi and Qfy, and therefore we tentatively suggest that the faults might had last ruptured in the middle to early Pleistocene. They have scarps up to 20 m, and assuming these have formed over the past 100 kyr, a Quaternary slip rate of ~0.2 mm/yr is calculated. Although reasonable, we emphasize that there are no quantitative ages for these surfaces. We also see no evidence for left-slip kinematics on these faults, as recorded in the online database. Their uphill facing character may reflect some oblique slip component or may simply result from their parallelism to the other major east-dipping normal faults observed across the study area. We note that several drainages exhibit right steps across the mapped faults, and therefore we suggest that the faults might involve some component of oblique right-lateral normal kinematics.

Summary

In this study, we conducted 1:24,000-scale geologic mapping in the northern Pine Nut Mountains coupled with new geochronological and geochemical analyses. The study area is located in the Carson Domain of the northern Walker Lane. The main rock units include Mesozoic basement rocks, an Oligocene ash-flow tuff, and Miocene-Pliocene basaltic andesite to dacite. A volcanic breccia in the Jurassic Gardnerville Formation yielded a ca. 177 Ma U-Pb zircon age, and two samples from the Miocene volcanic rocks yielded $^{40}Ar/^{39}Ar$ ages of 7.30-7.15 Ma. The Miocene-Pliocene volcanic rocks are geochemically similar to other Ancestral Cascade volcanic rocks in the Lake Tahoe and Reno, NV, region.

New mapping documented numerous north-striking east-dipping dip-slip normal faults, and a cross section across the study area suggests 3.3 km of west-east extension (17% extensional strain). Assuming that this deformation started sometime after the 7.15 Ma volcanic rock was deposited, the implied extension rate is 0.5 mm/yr. Along the western flank of the study area are north-striking fault scarps that cut Qfo horizons. Although these have been previously characterized as left-slip faults with activity within the last 15 ka, our observations suggest that they have been less active and may be oblique right-slip normal structures. We also show evidence for a previously unrecognized left-slip fault, which we name the Bull Canyon fault. It is not an active structure, but appears to kinematically link with the north-striking normal faults and may have accommodated 1-2 km of displacement.

There are several broader implications of this research. First, there may have been another left-slip fault in the Carson Domain that accommodated clockwise rotation of this region, similar to the Olinghouse and Wabuska faults. The newly identified Bull Canyon fault is no longer active, which suggests that during protracted block rotation the fault may have become a mechanically less favorable structure for slip and/or some fault-hardening process occurred. Second, this observation demonstrates that using large-scale geometrical properties of continental-scale fault networks—such as fault spacing and seismogenic zone thickness—can predict the location of inactive or previously unrecognized structures. Furthermore, these types of maps, which demonstrate the maximum depth of seismicity and represent proxies for crustal strength may be useful for future seismic hazards evaluation. Lastly, our work fits into the growing body of literature that shows that the westward encroachment of Basin and Range extension occurred in the Pine Nut Mountains after 7.15 Ma.

Products of funded research

Abstract

Say, M. C., and Zuza, A. V., 2019, Transitions between the Sierra Nevada, Basin and Range, and Walker Lane in the northern Pine Nut Mountains, Nevada: Insights from geologic mapping and Ar/Ar geochronology: Geological Society of America Abstracts with Programs, v51, no. 5.

Zuza, A. V., and Cao, W., 2019, Seismogenic thickness of California from earthquake-location data: Implications for thermal structure and seismic hazard: Geological Society of America Abstracts with Programs, v51, no. 5.

Manuscripts in review

Zuza, A. V., and Cao, W., in review, Seismogenic thickness of California: implications for thermal structure and seismic hazard: Tectonophysics.

Say, M. C., and Zuza, A. V., in review, Late Miocene transition between Basin and Range extension and Walker Lane tectonics, northern Pine Nut Mountains, Nevada: New insights from geologic mapping and $^{40}Ar/^{39}Ar$ geochronology: Proceedings of the Geological Society Nevada 2020 Meeting.

Acknowledgments: This work was supported by the National Earthquake Hazards Reduction Program (G18AP00082). The views and conclusions contained in this document are those of the authors and should not be interpreted as representing the opinions or policies of the U.S. Geological Survey. Mention of trade names or commercial products does not constitute their endorsement by the U.S. Geological Survey. Additional support for graduate student Michael Say was provided by the Nevada Petroleum and Geothermal Society and the Robert D. Hatcher Research Award from the Geological Society of America.

References

Bennett, R.A., Wernicke, B.P., Niemi, N.A., Friedrich, A.M., and Davis, J.L., 2003, Contemporary strain rates in the northern Basin and Range province from GPS data: Tectonics, v. 22, doi: 10.1029/2001TC001355.

Black, L. P., Kamo, S. L., Allen, C. M., Aleinikoff, J. N., Davis, D. W., Korsch, R. J., and Foudoulis, C., 2003, TEMORA 1: A new zircon standard for Phanerozoic U-Pb geochronology: Chemical Geology, v. 200, p. 155–170.

Bormann, J.M., Hammond, W.C., Kreemer, C., and Blewitt, G., 2016, Accommodation of missing shear strain in the Central Walker Lane, western North America: Constraints from dense GPS measurements: Earth and Planetary Science Letters, v. 440, p. 169-177.

Cashman, P.H., and Fontaine, S.A., 2000, Strain partitioning in the northern Walker Lane, western Nevada and northeastern California: Tectonophysics, v. 326, no. 1, p. 111-130.

Cashman, P. H., Trexler, J. H., Muntean, T. W., Faulds, J. E., Louie, J. N., and Oppliger, G. L., 2009, Neogene evolution of the Sierra Nevada-Basin and Range transition zone at the latitude of Carson City, Nevada, *in* Oldow, J. S., and Cashman, P. H., eds., Late Cenozoic structure and evolution of the Great Basin-Sierra Nevada transition: Geological Society of America Special Paper 447, p. 171–188.

Chiarabba, C., and De Gori, P., 2016, The seismogenic thickness in Italy: constraints on potential magnitude and seismic hazard: Terra Nova, v. 28, no. 6, p. 402-408.

Cousens, B., Prytulak, J., Henry, C., Alcazar, A., and Brownrigg, T., 2008, Geology, geochronology, and geochemistry of the Miocene–Pliocene Ancestral Cascades arc, northern Sierra Nevada, California and Nevada: The roles of the upper mantle, subducting slab, and the Sierra Nevada lithosphere: Geosphere, v. 4, no. 5, 829-853.

Dilles, J. H., and Gans, P. B., 1995, The chronology of Cenozoic volcanism and deformation in the Yerington area, western Basin and Range and Walker Lane: Geological Society of America Bulletin, v. 107, no. 4, p. 474-486.

Dilles, J. H., and Wright, J. E., 1988, The chronology of early Mesozoic arc magmatism in the Yerington district of western Nevada and its regional implications: Geological Society of America Bulletin, v. 100, no. 5, p. 644-652.

Dixon, T.H., Robaudo, S., Lee, J., and Reheis, M.C., 1995, Constraints on present-day Basin and Range deformation from space geodesy: Tectonics, v. 14, no. 4, p. 755-772.

Dixon, T.H., Miller, M., Farina, F., Wang, H., and Johnson, D., 2000, Present-day motion of the Sierra Nevada block and some tectonic implications for the Basin and Range province, North American Cordillera: Tectonics, v. 19, no. 1, p. 1-24.

Faulds, J.E., and Henry, C.D., 2008, Tectonic influences on the spatial and temporal evolution of the Walker Lane: An incipient transform fault along the evolving Pacific–North American plate boundary: Ores and orogenesis: Circum-Pacific tectonics, geologic evolution, and ore deposits: Arizona Geological Society Digest, v. 22, p. 437-470.

Fultz, L.A., Bell, E. J., and Trexler, D. T., 1984, Geochemistry, age and strontium isotope composition of late Tertiary and Quaternary basalts and andesites in western Nevada and their relation to geothermal potential: Final Report, Division of Earth Sciences, Environmental Research Center, University of Nevada, Las Vegas, 170 p.

Gross, M. R., Fischer, M. P., Engelder, T., and Greenfield, R. J., 1995, Factors controlling joint spacing in interbedded sedimentary rocks: integrating numerical models with field observations from the Monterey Formation, USA: Geological Society, London, Special Publications, v. 92, no. 1, p. 215-233.

Hammond, W.C., and Thatcher, W., 2007, Crustal deformation across the Sierra Nevada, northern Walker Lane, Basin and Range transition, western United States measured with GPS, 2000–2004: Journal of Geophysical Research: Solid Earth, v. 112, no. B5.

Hammond, W.C., Blewitt, G., and Kreemer, C., 2011, Block modeling of crustal deformation of the northern Walker Lane and Basin and Range from GPS velocities: Journal of Geophysical Research: Solid Earth, v. 116, no. B4.

DeMets, C., and Dixon, T. H., 1999, New kinematic models for Pacific-North America motion from 3 Ma to present, I: Evidence for steady motion and biases in the NUVEL-1A model: Geophysical Research Letters, v. 26, no.13, p. 1921-1924.

Harrison, T. M., 1982, Diffusion of 40 Ar in hornblende: Contributions to Mineralogy and Petrology, v. 78, no. 3, p. 324-331.

Hauksson, E., Yang, W., and Shearer, P.M., 2012, Waveform relocated earthquake catalog for southern California (1981 to June 2011): Bulletin of the Seismological Society of America, v. 102, no. 5, p. 2239-2244.

Henry, C.D., and Faulds, J.E., 2007, Geometry and timing of strike-slip and normal faults in the northern Walker Lane, northwestern Nevada and northeastern California: Strain partitioning or sequential extensional and strike-slip deformation?: Geological Society of America Special Papers, v. 434, p. 59-79.

Henry, C. D., and Perkins, M. E., 2001, Sierra Nevada–Basin and Range transition near Reno, Nevada: two-stage development at 12 and 3 Ma: Geology, v. 29, no. 8, p. 719-722.

Henry, C. D., Castor, S. B., Starkel, W. A., Ellis, B. S., Wolff, J. A., Laravie, J. A., McIntosh, W. C., and Heizler, M. T., 2017, Geology and evolution of the McDermitt caldera, northern Nevada and southeastern Oregon, western USA: Geosphere, v. 13, no. 4, p. 1066-1112.

Henry, C. D., Hinz, N. H., Faulds, J. E., Colgan, J. P., John, D. A., Brooks, E. R., Cassel, E. J., Garside, L., Davis, D. A., and Castor, S. B., 2012, Eocene–Early Miocene paleotopography of the Sierra Nevada–Great Basin–Nevadaplano based on widespread ash-flow tuffs and paleovalleys: Geosphere, v. 8, no. 1, p. 1-27.

Hobbs, D. W., 1967, The formation of tension joints in sedimentary rocks: an explanation: Geological Magazine, v. 104, no. 6, p. 550-556.

Irvine, T. N. J., and Baragar, W. R. A., 1971, A guide to the chemical classification of the common volcanic rocks: Canadian journal of earth sciences, v. 8, no. 5, p. 523-548.

Kreemer, C., Hammond, W. C., Blewitt, G., Hollad, A. A., and Bennet, R. A., 2012, geodetic strain rate model for the Pacific–North American plate boundary, western United States: Nevada Bureau of Mines and Geology Map 178,

Kuiper, K. F., Deino, A., Hilgen, F. J., Krijgsman, W., Renne, P. R., and Wijbrans, A. J., 2008, Synchronizing rock clocks of Earth history: Science, v. 320, no. 5875, p. 500-504.

Lachenbruch, A. H., 1961, Depth and spacing of tension cracks: Journal of Geophysical Research, v. 66, no. 12, p. 4273-4292.

Bas, M. L., Maitre, R. L., Streckeisen, A., Zanettin, B., and IUGS Subcommission on the Systematics of Igneous Rocks, 1986, A chemical classification of volcanic rocks based on the total alkali-silica diagram: Journal of Petrology, v. 27, no. 3, p. 745-750.

Li, X., Huang, W., Pierce, I. K., Angster, S. J., and Wesnousky, S. G., 2017, Characterizing the Quaternary expression of active faulting along the Olinghouse, Carson, and Wabuska lineaments of the Walker Lane: Geosphere, v. 13, no. 6, p. 2119-2136.

Lin, G., Shearer, P. M., and Hauksson, E., 2007, Applying a three-dimensional velocity model, waveform cross correlation, and cluster analysis to locate southern California seismicity from 1981 to 2005: Journal of Geophysical Research: Solid Earth, v. 112, no. B12.

Long, S. P., 2018, Geometry and magnitude of extension in the Basin and Range Province (39° N), Utah, Nevada, and California, USA: Constraints from a province-scale cross section: GSA Bulletin, v. 131, no. 1-2, p. 99-119.

Ludwig, K. I., 2012, Isoplot 3.75: A geochronological toolkit for Microsoft Excel: Berkeley Geochronology Center Special Publication, v. 4.

McDougall, I., and Harrison, T. M., 1999, Geochronology and Thermochronology by the $^{40}Ar/^{39}Ar$ Method. Oxford University Press.

McIntosh, W. C., Heizler, M., Peters, L., and Esser, R., 2003, $^{40}Ar/^{39}Ar$ geochronology at the New Mexico Bureau of Geology and Mineral Resources. Socorro, New Mexico Bureau of Geology and Mineral Resources: Open File Report OF-AR-1.

Narr, W., and Suppe, J., 1991, Joint spacing in sedimentary rocks: Journal of Structural Geology, v. 13, no. 9, p. 1037-1048.

Noble, D.C., 1962, Mesozoic geology of the southern Pine Nut Range, Douglas County, Nevada (PhD dissertation): Stanford, California, Stanford University, 200 p.

Oldow, J. S., Aiken, C. L. V., Hare, J. L., Ferguson, J. F., and Hardyman, R. F., 2001), Active displacement transfer and differential block motion within the central Walker Lane, western Great Basin: Geology, v. 29, no. 1, p. 19-22.

Russell, K., 1981, Geology and ore deposits of the Como mining district, Lyon County, Nevada (MS thesis): Fresno, California State University, 85 p.

Schaff, D. P., and Waldhauser, F., 2005, Waveform cross-correlation-based differential travel-time measurements at the Northern California Seismic Network: Bulletin of the Seismological Society of America, v. 95, no.6, p. 2446-2461.

Schweickert, R. A., 1978, Triassic and Jurassic paleogeography of the Sierra Nevada and adjacent regions, California and western Nevada *in* Howell, D.G., and McDougall, K.A., eds., Mesozoic paleogeography of the western United States: Los Angeles, Society of Economic Paleontologists and Mineralogists, Pacific Section Pacific Coast Paleogeography Symposium 2, p. 361–384.

Sibson, R. H., 1982, Fault zone models, heat flow, and the depth distribution of earthquakes in the continental crust of the United States: Bulletin of the Seismological Society of America, v. 72, no. 1, p. 151-163.

Sláma, J., Košler, J., Condon, D. J., Crowley, J. L., Gerdes, A., Hanchar, J. M., Horstwood, M. S. A., Morris, G. A., Nasdala, L., Norbeg, N., Schaltegger, U., Schoene, B., Tubrett, M.

N., and Whitehouse, M. J., 2008, Plešovice zircon—a new natural reference material for U–Pb and Hf isotopic microanalysis: Chemical Geology, v. 249, no. 1-2, p. 1-35.

Slemmons, D.B., Van Wormer, D., Bell, E.J., and Silberman, M.L., 1979, Recent crustal movements in the Sierra Nevada—Walker lane region of California—Nevada: Part i, rate and style of deformation: Tectonophysics, v. 52, no. 1-4, p. 561-570.

Steiger, R., & Jäger, E., 1977, Subcommission on geochronology: convention on the use of decay constants in geo- and cosmochronology. Earth and Planetary Science Letters, v. 36, no. 3, p. 359-362.

Stewart, J.H., 1980, Regional tilt patterns of late Cenozoic basin-range fault blocks, western United States: Geological Society of America Bulletin, v. 91, no. 8, p. 460-464.

Stewart, J.H., 1988, Tectonics of the Walker Lane belt, western Great Basin: Mesozoic and Cenozoic deformation in a zone of shear. In: Metamorphism and crustal evolution of the western United States (W.G. Ernst, ed.): Prentice Hall, New Jersey, p. 681-713.

Stewart, J.H., 1997, Triassic and Jurassic stratigraphy and paleontology of west-central Nevada and eastern California: U.S. Geological Survey Open- File Report 97-495, 37 p.

Stewart, J.H., 1999, Geologic Map of the Carson City 30 x 60 Minute Quadrangle, Nevada: Nevada Bureau of Mines and Geology.

Sun, S. S., and McDonough, W. F., 1989, Chemical and isotopic systematics of oceanic basalts: implications for mantle composition and processes: Geological Society, London, Special Publications, v. 42, no. 1, p. 313-345.

Sturmer, D. M., and Faulds, J. E., 2018, Kinematic evolution of the Olinghouse fault and the role of a major sinistral fault in the Walker Lane dextral shear zone, Nevada, USA: Journal of Structural Geology, v. 115, p. 47-63.

Surpless, B.E., Stockli, D.F., Dumitru, T.A., and Miller, E.L., 2002, Two-phase westward encroachment of Basin and Range extension into the northern Sierra Nevada: Tectonics, v. 21, no. 1.

Taylor, J.R., 1982, An introduction to error analysis: Mill Valley, California, University Science Books, 270 p.

Thatcher, W., Savage, J.C., and Simpson, R.W., 2016, The Eastern California Shear Zone as the northward extension of the southern San Andreas fault: Journal of Geophysical Research: Solid Earth, v. 121, p. 2904-2914.

Thatcher, W., 2003, GPS constraints on the kinematics of continental deformation: International Geology Review, v. 45, no. 3, p. 191-212.

Unruh, J., Humphrey, J., and Barron, A., 2003, Transtensional model for the Sierra Nevada frontal fault system, eastern California: Geology, v. 31, no. 4, p. 327-330.

Vikre, P. G., and McKee, E. H., 1994, Geology, alteration, and geochronology of the Como District, Lyon County, Nevada: Economic Geology, v. 89, no. 3, p. 639-646.

Waldhauser, F., and Schaff, D. P., 2008, Large-scale relocation of two decades of northern California seismicity using cross-correlation and double-difference methods: Journal of Geophysical Research: Solid Earth, v. 113, no. B8.

Wesnousky, S.G., 2005a, Active faulting in the Walker Lane: Tectonics, v. 24, no. 3.

Wesnousky, S.G., 2005b, The San Andreas and Walker Lane fault systems, western North America: Transpression, transtension, cumulative slip and the structural evolution of a major transform plate boundary: Journal of Structural Geology, v. 27, no. 8, p. 1505-1512.

Wesnousky, S.G., Bormann, J.M., Kreemer, C., Hammond, W.C., and Brune, J.N., 2012, Neotectonics, geodesy, and seismic hazard in the Northern Walker Lane of Western North America: Thirty kilometers of crustal shear and no strike-slip?: Earth and Planetary Science Letters, v. 329, p. 133-140.

Wiedenbeck, M., Hanchar, J. M., Peck, W. H., Sylvester, P., Valley, J., Whitehouse, M., Kronz, A., Morishita, Y., Nasdala, L., Fiebig, J., Franchi, I., Girard, J. P., Greenwod, R. C., Hinton, R., Kita, N., Mason, P. R. D., Norman, M., Ogasawara, M., Piccoli, P. M., Rhede, D., Satoh, H., Schulz-Dobrick, B., Skar, O., Spicuzza, M. J., Terada, K., Tindle, A., Togashi, S., Vennemann, T., Xie, Q., and Zheng, Y. F., 2004, Further characterisation of the 91500 zircon crystal: Geostandards and Geoanalytical Research, v. 28, no. 1, p. 9-39.

Yang, H., Moresi, L. N., and Quigley, M., 2019, Fault spacing in continental strike-slip shear zones: Earth and Planetary Science Letters, in press.

Yin, A., Zuza, A. V., and Pappalardo, R. T., 2016, Mechanics of evenly spaced strike-slip faults and its implications for the formation of tiger-stripe fractures on Saturn's moon Enceladus: Icarus, v. 266, p. 204-216.

Zuza, A. V. and Cao., W., in review, Seismogenic thickness of California: implications for thermal structure and seismic hazard: Tectonophysics.

Zuza, A. V., and Carlson, C. W., 2018, What can strike-slip fault spacing tell us about the plate boundary of western North America?: Terra Nova, v. 30, no. 2, p. 105-113.

Zuza, A.V., Yin, A., Lin, J., and Ming, S., 2017, Spacing and strength of active continental strike-slip faults: EPSL, v. 457, p. 49-62.

Appendix Table 1. Whole-rock geochemical compositions of northern Pine Nut Mountains Miocene volcanic rocks

Unit:	Tac							Tad					
Sample:	**MS-270918-1**	**MS-070419-1**	**MS-210619-2**	**MS-220619-1**	**MS-261018-8**	**MS-261018-7**	**MS-261018-4**	**MS-261018-5**	**MS-261018-2**	**MS-261018-11**	**MS-261018-10**	**MS-261018-9**	**MS-230619-2**
Lat (°N)	39.1890	39.1970	39.2146	39.2137	39.1790	39.1690	39.1690	39.1718	39.1606	39.2071	39.2055	39.1928	39.2007
Long (°W)	119.4503	119.4438	119.4361	119.4341	119.4790	119.4930	119.5009	119.5099	119.5180	119.4592	119.4583	119.4669	119.4811
Major and minor elements (wt%)													
SiO_2	61.1	56.3	59.5	56.5	59.8	56.6	57.0	59.3	61.1	62.3	62.9	62.8	61.0
Al_2O_3	16.70	17.3	17.55	17.45	16.30	17.60	17.60	17.95	17.25	16.30	16.75	17.95	17.35
Fe_2O_3	5.60	7.27	6.52	5.93	5.60	7.37	6.51	6.54	5.51	5.11	5.22	5.34	5.69
CaO	5.93	6.26	6.26	7.08	5.40	6.54	6.72	5.92	5.23	4.45	4.62	4.03	5.39
MgO	2.51	3.23	3.13	1.9	3.28	3.66	3.15	3.17	2.80	1.64	1.84	1.54	1.98
Na_2O	3.67	3.65	3.37	3.73	3.38	3.23	3.55	3.69	4.18	3.29	3.63	3.74	4.08
K_2O	2.16	1.57	2.12	1.72	1.17	1.51	1.49	1.62	1.67	2.13	2.15	1.95	1.97
Cr_2O_3	0.00	0.00	0.00	0.00	0.00	0.01	0.01	0.00	0.00	0.00	0.00	0.00	0.00
TiO_2	0.70	0.8	0.78	0.71	0.68	0.95	0.81	0.75	0.66	0.58	0.60	0.67	0.6
MnO	0.13	0.11	0.11	0.15	0.11	0.11	0.08	0.11	0.10	0.07	0.06	0.04	0.12
P_2O_5	0.23	0.26	0.27	0.23	0.23	0.32	0.26	0.26	0.23	0.19	0.19	0.23	0.22
SrO	0.10	0.09	0.1	0.09	0.10	0.10	0.10	0.10	0.10	0.08	0.08	0.08	0.08
BaO	0.12	0.1	0.09	0.1	0.12	0.12	0.11	0.11	0.13	0.15	0.13	0.12	0.11
LOI	1.44	2.06	2.02	3.8	4.52	2.93	3.89	2.47	0.85	4.97	3.48	2.85	0.98
Total	100.39	99	101.82	99.39	100.69	101.05	101.28	101.99	99.81	101.26	101.65	101.34	99.57
Trace elements (ppm)													
Ba	1010	883	854	945	1060	1075	1010	974	1145	1285	1130	1015	1020
Ce	39.8	36.7	37	34.7	34.6	38.4	36.4	33.6	34.8	37.2	37.9	38.8	34.8
Cr	20	30	30	20	20	40	40	30	20	20	20	20	20
Cs	0.64	1.5	2.82	0.63	0.44	0.46	1.36	1.12	0.56	4.27	1.71	0.83	0.64
Dy	2.6	2.85	3.02	2.68	2.37	3.31	2.48	2.59	2.37	2.04	2.11	2.21	2.56
Er	1.31	1.69	1.64	1.42	1.37	1.99	1.51	1.51	1.46	1.18	1.22	1.17	1.48
Eu	1.13	1.08	0.99	1.08	1.02	1.32	1.11	1.13	1.04	0.82	0.96	1.04	1.03
Ga	19.9	19.1	20.7	21.8	19.3	20.9	20.5	21.7	20.7	18.8	19.4	20.9	19.2
Gd	3.18	3.55	3.27	3.08	3.18	3.92	3.65	3.24	3.06	2.72	2.74	3.0	3.05
Hf	3.3	3.2	3.7	3.1	3.1	3	3.4	2.9	3.2	3.5	3.4	3.7	3
Ho	0.54	0.51	0.56	0.51	0.49	0.64	0.48	0.48	0.51	0.43	0.46	0.42	0.6
La	19.7	18.6	19.1	18.1	17.2	18.1	17.8	16.4	17.6	18.7	19.3	19.4	20.2
Lu	0.23	0.21	0.19	0.21	0.21	0.24	0.18	0.21	0.21	0.17	0.19	0.19	0.27
Nb	4.8	4.4	4.6	4.5	4.4	4.7	4.4	4.2	4.2	4.3	4.6	5.1	4.6
Nd	19.7	20	20.5	18.8	18.3	21	19.2	18.3	18.3	16.9	17.9	18.3	19.4
Pr	5.05	4.76	5.05	4.55	4.45	5	4.66	4.36	4.42	4.55	4.65	4.81	4.89
Rb	40.4	23.2	36	31.9	27.8	22	24.8	27.2	21	43.4	39.5	33.2	32.6
Sm	3.71	3.85	4.25	4.08	3.73	4.37	4.04	3.76	3.98	3.62	3.41	3.78	3.85
Sn	1	1	1	1	1	1	1	1	1	1	1	1	1
Sr	745	759	804	760	812	795	832	871	818	679	708	627	664
Ta	0.4	0.3	0.4	0.4	0.4	0.4	0.4	0.3	0.4	0.4	0.4	0.4	0.4
Tb	0.46	0.46	0.45	0.51	0.44	0.6	0.53	0.49	0.47	0.34	0.38	0.41	0.5
Th	3.42	3.8	2.84	3.34	2.59	2.14	2.15	2.1	2.66	4.01	3.84	2.99	3.46
Tm	0.19	0.25	0.22	0.17	0.22	0.28	0.23	0.2	0.21	0.18	0.18	0.18	0.24
U	1.28	1.09	1.15	1.48	1.21	0.86	0.91	0.87	0.83	1.35	1.12	1.19	1.35
V	126	144	143	140	126	193	161	149	90	87	85	144	121
W	1	1	1	2	1	1	1	1	1	1	1	1	1
Y	14	14.8	14.6	13.9	13.8	17.1	14.8	14	13.7	11.7	12.2	12	16.7
Yb	1.4	1.33	1.32	1.35	1.4	1.83	1.46	1.35	1.36	1.19	1.22	1.09	1.78
Zr	121	114	117	106	120	126	122	112	126	124	116	138	111

Appendix Table 1 (cont.). Whole-rock geochemical compositions of northern Pine Nut Mountains Miocene volcanic rocks

Unit:	Tad						Tai	Tdi					Tbt
Sample:	**MS-261018-1**	**MS-030819-1**	**MS-020819-4**	**MS-080719-1**	**MS-070819-4**	**MS-240819-6**	**MS-060719-4**	**MS-261018-3**	**MS-060419-4**	**MS-240819-4**	**MS-240819-5**	**MS-010819-1**	**MS-070719-2**
Lat (°N)	39.1789	39.2042	39.2023	39.2204	39.1869	39.2457	39.2201	39.1626	39.1950	39.2313	39.2345	39.1834	39.2209
Long (°W)	119.5295	119.5138	119.4571	119.4118	119.4293	119.5024	119.4528	119.5123	119.4475	119.4442	119.4489	119.4617	119.4285
Major and minor elements (wt%)													
SiO_2	62.0	61.0	60.4	61.3	60.1	64.0	59.5	60.9	64.7	60.0	64.2	59.9	67.0
Al_2O_3	17.05	17.3	16.6	17.05	17	16.2	17.05	18.15	16.25	16.5	16.9	16.75	16.05
Fe_2O_3	5.54	5.56	4.82	5.72	6.61	4.15	5.75	5.97	5.07	5.34	5.64	6.34	3.75
CaO	5.20	5.25	4.2	4.83	6.21	4.01	5.6	5.99	4.57	5.52	4.76	5.18	2.61
MgO	2.40	1.94	2.48	1.85	3.26	1.22	2.65	2.83	2.33	2.36	0.48	2.95	0.8
Na_2O	3.87	4.18	3.51	3.95	3.51	4.15	3.81	4.27	3.79	3.84	3.74	3.5	3.49
K_2O	1.89	2.03	2.2	2.21	1.98	2.73	1.92	1.59	2.45	2.26	1.9	1.95	4.84
Cr_2O_3	0.00	0.00	<0.002	<0.002	0.00	0.00	0.01	0.00	0.00	0.00	0.00	0.00	<0.002
TiO_2	0.67	0.68	0.59	0.64	0.67	0.46	0.66	0.74	0.56	0.63	0.66	0.86	0.43
MnO	0.09	0.1	0.07	0.11	0.11	0.05	0.15	0.10	0.08	0.07	0.03	0.09	0.03
P_2O_5	0.43	0.29	0.22	0.24	0.26	0.24	0.22	0.24	0.2	0.23	0.21	0.39	0.16
SrO	0.09	0.1	0.07	0.08	0.08	0.08	0.08	0.10	0.07	0.09	0.08	0.11	0.06
BaO	0.14	0.13	0.13	0.15	0.1	0.13	0.11	0.11	0.13	0.12	0.12	0.14	0.17
LOI	1.67	1.11	4.23	1.38	1.7	1.27	1.83	0.85	1.63	2.29	1.17	3.63	1.07
Total	101.04	99.67	99.52	99.51	101.59	98.69	99.34	101.84	101.83	99.25	99.89	101.79	100.46
Trace elements (ppm)													
Ba	1220	1150	1150	1325	946	1165	1035	1030	1165	1130	1095	1225	1585
Ce	38	38.3	36.6	37.1	32.5	40.1	34.5	31.7	33.5	37	33.1	39.6	56.9
Cr	30	30	10	20	30	20	40	20	20	20	20	20	10
Cs	0.73	1.07	0.77	0.83	1.51	2.12	1.08	0.85	0.71	0.78	5.61	0.48	1.13
Dy	2.31	2.75	2.04	2.53	3.13	2.33	2.61	2.52	2.36	2.32	2.34	2.84	2.87
Er	1.37	1.46	1.26	1.4	1.64	1.22	1.37	1.37	1.25	1.47	1.36	1.41	1.87
Eu	1.03	1.06	0.96	1.01	1.21	0.72	0.96	1.1	0.74	1.02	0.9	1.14	0.89
Ga	20.1	22.1	20	19.8	20.2	19.6	21.3	21.4	17.5	21.4	20.6	20.5	19.6
Gd	2.94	2.81	2.8	3.2	3.31	2.75	2.72	3.1	2.72	2.92	2.71	3.62	3.53
Hf	3.4	3.7	3.5	3.5	3	3.4	3.4	2.9	4	3.6	3.3	3.6	5.3
Ho	0.44	0.51	0.38	0.48	0.64	0.46	0.54	0.51	0.46	0.46	0.44	0.49	0.6
La	18.1	21.7	18.7	19.7	18.4	22.9	18.3	15.6	18	19.7	17.3	19.9	31.8
Lu	0.18	0.2	0.18	0.24	0.26	0.17	0.21	0.21	0.21	0.2	0.2	0.17	0.29
Nb	4.6	5.2	4.2	5.1	4.3	5.1	4	4	4.5	4.7	4.4	5.6	9.5
Nd	18.2	19.2	18	18.5	18.9	19.1	17.9	17.9	15.6	18.8	17.3	21.7	25.9
Pr	4.56	4.87	4.47	4.77	4.71	5.02	4.48	4.2	4.1	4.74	4.34	5.15	6.66
Rb	23.5	32.9	23.2	37.4	31.1	56.8	33.3	26.1	41.3	39.8	32.6	29.2	118
Sm	3.75	4.23	3.28	3.43	4.34	3.82	3.85	3.79	3.2	3.86	3.46	4.65	4.48
Sn	1	2	1	1	1	1	1	1	1	1	1	1	2
Sr	760	797	591	665	659	658	707	893	586	776	669	886	528
Ta	0.4	0.4	0.4	0.4	0.4	0.5	0.4	0.3	0.5	0.4	0.4	0.5	1
Tb	0.4	0.39	0.4	0.45	0.51	0.4	0.4	0.48	0.38	0.44	0.38	0.45	0.44
Th	3.26	3.22	3.62	3.67	2.81	6.49	3.41	2.01	4.9	3.56	2.71	3.42	14
Tm	0.2	0.18	0.16	0.22	0.26	0.2	0.18	0.21	0.2	0.19	0.19	0.21	0.25
U	1.17	1.46	1.54	1.45	1.97	2.84	1.34	0.99	1.71	1.51	0.96	1.36	3.06
V	123	246	106	110	147	80	129	150	107	119	116	131	47
W	1	3	1	1	1	1	1	1	1	1	1	1	4
Y	12.4	14	11.5	14.3	16.2	13.4	13.2	13.7	12.1	13.4	12.3	13.9	17.8
Yb	1.35	1.27	1.21	1.47	1.82	1.31	1.28	1.49	1.34	1.27	1.23	1.22	1.94
Zr	135	128	122	133	101	118	122	113	126	122	121	127	187

Appendix Table 1 (cont.). Whole-rock geochemical compositions of northern Pine Nut Mountains Miocene volcanic rocks

Unit:	Tba				Tbay		Ta		Tdo		
Sample:	**MS-110719-1**	**MS-070719-4**	**MS-110719-2**	**MS-240819-3**	**MS-220918-1**	**MS-120719-1**	**MS-070819-3**	**MS-110719-4**	**MS-220918-10**	**MS-240819-1**	**MS-220918-6**
Lat (°N)	39.2314	39.2292	39.2353	39.2346	39.2424	39.2418	39.2135	39.2252	39.2191	39.2237	39.2200
Long (°W)	119.4210	119.4323	119.4276	119.4336	119.3930	119.4050	119.4323	119.4151	119.4249	119.4308	119.4254
Major and minor elements (wt%)											
SiO_2	62.7	54.4	57.0	57.8	56.2	56.3	57.6	58.8	64.0	59.4	61.8
Al_2O_3	16	17.95	17.35	17.4	18.85	18.65	17.6	17.25	15.45	17.55	16.00
Fe_2O_3	4.64	7.85	7.03	6.88	7.20	7.11	6.39	6.38	4.74	6.38	5.16
CaO	3.73	6.96	6.16	6.38	7.48	7.81	7.11	7	4.94	5.42	4.44
MgO	1.38	3.32	3.06	2.88	2.85	3.11	2.56	1.34	1.35	2.08	2.24
Na_2O	3.99	3.74	3.76	3.81	3.89	3.83	3.79	3.56	3.32	3.88	3.55
K_2O	2.26	1.45	1.54	1.51	1.33	1.4	1.53	1.77	2.69	1.74	2.53
Cr_2O_3	<0.002	0.00	0.00	0.00	0.00	0.00	0.00	0.00	0.00	0.00	0.00
TiO_2	0.51	1	0.77	0.75	0.79	0.8	0.79	0.67	0.49	0.74	0.53
MnO	0.04	0.13	0.1	0.13	0.11	0.17	0.11	0.11	0.09	0.03	0.08
P_2O_5	0.19	0.41	0.26	0.29	0.32	0.37	0.26	0.23	0.16	0.28	0.19
SrO	0.08	0.1	0.11	0.11	0.16	0.17	0.1	0.09	0.06	0.1	0.07
BaO	0.14	0.11	0.12	0.12	0.09	0.1	0.11	0.14	0.13	0.13	0.12
LOI	2.45	1.63	1.68	1.14	0.86	1.03	2.8	4.15	4.10	3.13	1.96
Total	98.11	99.05	98.94	99.2	100.13	100.85	100.75	101.49	101.52	100.86	98.67
Trace elements (ppm)											
Ba	1305	1005	1035	1080	774	966	935	1265	1135	1175	1055
Ce	33.4	41.8	35.3	35.1	43.6	49.7	38.2	33.9	40	38	47.9
Cr	10	30	30	30	20	20	30	40	20	30	20
Cs	1.51	0.93	0.74	1.07	3.16	6.21	1.01	1.45	2.28	0.21	1.94
Dy	1.76	3.82	2.82	2.57	2.94	2.94	2.95	2.53	2.38	2.87	2.35
Er	0.87	2.17	1.52	1.66	1.57	1.49	1.63	1.41	1.38	1.52	1.35
Eu	0.76	1.54	1.11	1.03	1.29	1.43	1.15	0.91	0.88	1.25	0.94
Ga	21.1	21.5	20.7	21.1	21.9	24.5	22.9	20.6	17.5	20.9	18
Gd	2.05	4.42	3.48	3.73	3.71	4.24	3.28	3.31	2.79	3.41	2.9
Hf	3.3	3.4	3	3	2.9	2.8	3.2	3.1	3.2	3.2	3.6
Ho	0.29	0.73	0.53	0.55	0.55	0.59	0.61	0.56	0.53	0.52	0.51
La	18.8	20.7	19.1	19.9	20.1	25.9	19.2	17.4	21.9	19.7	25.7
Lu	0.15	0.27	0.21	0.22	0.21	0.23	0.22	0.22	0.22	0.18	0.23
Nb	4.6	6.1	4.4	4.2	3.7	3.7	4.4	4.3	4.7	4.8	4.8
Nd	14.9	25	19.9	19.7	23.8	26	20	17.6	17.6	20.2	20.2
Pr	4.04	5.93	4.99	4.71	5.71	6.6	4.86	4.47	4.64	4.96	5.62
Rb	44	22.3	24	24.7	15.6	33.1	24.2	30.5	66.3	16.6	65.1
Sm	2.71	5.22	4.56	4.31	4.84	5.37	4.48	3.99	3.31	3.79	3.72
Sn	1	1	1	1	1	1	1	1	1	1	1
Sr	631	814	863	901	1290	1395	823	705	509	834	599
Ta	0.4	0.4	0.3	0.3	0.3	0.3	0.4	0.4	0.5	0.4	0.5
Tb	0.3	0.62	0.43	0.53	0.49	0.53	0.51	0.43	0.43	0.49	0.4
Th	4.14	1.83	3.59	3.66	2.54	4.6	2.62	2.67	7.72	3.12	8.7
Tm	0.15	0.29	0.22	0.21	0.21	0.2	0.23	0.2	0.21	0.21	0.21
U	1.45	0.69	1.35	1.31	0.73	1.56	1.12	1.12	2.67	0.95	2.85
V	79	168	146	148	170	170	147	140	103	121	118
W	1	1	1	1	1	<1	1	1	1	1	1
Y	8.8	19.7	15.4	15.9	15.5	15.5	14	13.9	15	14.2	13.4
Yb	0.97	2.22	1.36	1.43	1.48	1.38	1.55	1.2	1.37	1.44	1.33
Zr	118	123	105	107	99	103	121	123	109	118	125

Appendix Table 2. $^{40}Ar/^{39}Ar$ analytical data.

	ID	Power (Watts)	$^{40}Ar/^{39}Ar$	$^{37}Ar/^{39}Ar$	$^{36}Ar/^{39}Ar$ (x 10^{-3})	$^{39}Ar_K$ (x 10^{-15} mol)	K/Ca	$^{40}Ar^*$ (%)	^{39}Ar (%)	Age (Ma)	±1σ (Ma)
	MS261018-2, Hornblende, 10.68 mg, J=0.0014928±0.02%, D=1±0, NM-303C, Lab#=66830-01										
	Lower Dacite (Tad)										
	A	1.5	18.82	3.894	55.38	1.3	0.13	14.7	6.2	7.57	0.30
	B	2.0	10.32	7.198	27.68	1.8	0.071	26.3	14.7	7.45	0.18
	C	2.5	9.033	8.322	24.00	2.8	0.061	28.8	27.7	7.15	0.13
	D	3.0	9.299	8.544	25.09	2.8	0.060	27.6	40.9	7.05	0.15
	E	3.5	8.407	8.970	21.97	2.6	0.057	31.3	52.7	7.22	0.13
	F	4.0	8.957	9.643	24.20	1.8	0.053	28.8	60.9	7.07	0.17
	G	4.5	8.588	10.17	22.99	1.8	0.050	30.3	69.2	7.16	0.17
	H	5.0	8.703	10.97	23.42	1.2	0.046	30.6	74.7	7.31	0.23
	I	5.5	9.582	10.99	27.04	0.9	0.046	25.8	78.7	6.78	0.27
	J	6.0	9.583	12.29	26.61	0.6	0.042	28.2	81.5	7.43	0.34
	K	6.5	11.13	12.69	32.17	0.5	0.040	23.7	84.1	7.26	0.40
	L	15.0	10.42	10.98	29.67	3.4	0.046	24.3	100.0	6.96	0.13
	Integrated age ± 2σ			n=12		21.5	0.055	K2O=0.52%		7.17	0.11
	Plateau ± 2σ	steps A-L		n=12	MSWD=0.98	21.5	0.059±0.049		100.0	7.15	0.10
	Isochron±2σ	steps A-L		n=12	MSWD=0.96		$^{40}Ar/^{36}Ar$=	299.0±6.4		6.93	0.42
	MS270918-1, Hornblende, 9.66 mg, J=0.0014978±0.02%, D=1±0, NM-303C, Lab#=66831-01										
	Como Andesite (Tac)										
X	A	1.5	386.2	9.107	1320.9	0.2	0.056	-0.9	1.1	-9.4	4.0
	B	2.0	11.38	11.59	33.24	0.9	0.044	21.8	6.2	6.86	0.29
	C	2.5	5.295	11.37	11.85	1.9	0.045	51.0	17.2	7.45	0.13
	D	3.0	5.635	11.32	13.01	1.9	0.045	47.8	28.3	7.43	0.13
	E	4.0	5.556	11.39	13.00	2.7	0.045	47.2	44.0	7.24	0.10
	F	4.5	5.321	11.49	12.38	2.3	0.044	48.5	57.2	7.11	0.12
	G	5.0	4.817	11.62	10.29	2.2	0.044	56.1	69.7	7.45	0.11
	H	6.0	5.292	11.96	12.30	1.5	0.043	49.4	78.4	7.21	0.14
	I	7.0	5.195	11.59	11.73	1.1	0.044	51.1	84.9	7.32	0.17
	J	15.0	5.582	11.79	13.15	2.6	0.043	47.3	100.0	7.28	0.10
	Integrated age ± 2σ			n=10		17.1	0.044	K2O=0.45%		7.11	0.12
	Plateau ± 2σ	steps B-J		n=9	MSWD=1.26	16.9	0.044±0.002		98.9	7.300	0.094
	Isochron±2σ	steps B-J		n=9	MSWD=1.01		$^{40}Ar/^{36}Ar$=	286.9±9.5		7.53	0.26

Notes:

Isotopic ratios corrected for blank, radioactive decay, and mass discrimination, not corrected for interfering reactions.
Errors quoted for individual analyses include analytical error only, without interfering reaction or J uncertainties.
Integrated age calculated by summing isotopic measurements of all steps.
Integrated age error calculated by quadratically combining errors of isotopic measurements of all steps.
Plateau age is inverse-variance-weighted mean of selected steps.
Plateau age error is inverse-variance-weighted mean error (Taylor, 1982) times root MSWD where MSWD>1.
Plateau error is weighted error of Taylor (1982).
Decay constants and isotopic abundances after Steiger and Jäger (1977).
X symbol preceding sample ID denotes analyses excluded from plateau age calculations.
Weight percent K_2O calculated from ^{39}Ar signal, sample weight, and instrument sensitivity.
Ages calculated relative to FC-2 Fish Canyon Tuff sanidine interlaboratory standard at 28.201 Ma (Kuiper et al., 2008)
Decay Constant (LambdaK (total)) = 5.463e-10/a
Correction factors:
$(^{39}Ar/^{37}Ar)_{Ca}$ = 0.0006926 ± 0.000016
$(^{36}Ar/^{37}Ar)_{Ca}$ = 0.0002702 ± 0.0000010
$(^{38}Ar/^{39}Ar)_{K}$ = 0.0121
$(^{40}Ar/^{39}Ar)_{K}$ = 0.000129 ± 8e-05

Appendix Table 3. Zircon U-Pb information for Gardnerville Formation sample MS-220918-9

	Ratios						Ages (Ma)							
ID	$^{206}Pb/^{238}U$	$^{206}Pb/^{238}U$ (2SE)	$^{207}Pb/^{235}U$	$^{207}Pb/^{235}U$ (2SE)	$^{207}Pb/^{206}Pb$	$^{207}Pb/^{206}Pb$ (2SE)	$^{206}Pb/^{238}U$	$^{206}Pb/^{238}U$ (2SE)	$^{207}Pb/^{235}U$	$^{207}Pb/^{235}U$ (2SE)	$^{207}Pb/^{206}Pb$	$^{207}Pb/^{206}Pb$ (2SE)	Conc.	Ex.*
1	0.02878	0.00065	0.19063	0.01330	0.04845	0.00288	182.90	4.09	176.32	11.14	118.54	35.00	1.04	
2	0.02818	0.00068	0.21658	0.01436	0.05419	0.00313	179.16	4.24	198.11	11.97	103.83	35.36	0.90	
3	0.02670	0.00101	0.20377	0.01141	0.05735	0.00352	169.83	6.32	189.83	10.36	110.00	37.82	0.89	x
4	0.02889	0.00069	0.20092	0.01235	0.05174	0.00312	183.58	4.30	185.18	10.39	103.42	34.88	0.99	
5	0.02816	0.00073	0.19099	0.01083	0.04950	0.00258	179.00	4.57	176.89	9.25	85.67	35.84	1.01	
6	0.02895	0.00075	0.19161	0.01148	0.05010	0.00324	183.95	4.68	177.36	9.76	106.06	34.86	1.04	
7	0.02933	0.00082	0.19415	0.01444	0.04880	0.00355	186.30	5.11	179.16	12.32	88.73	34.46	1.04	
8	0.02747	0.00068	0.18604	0.01156	0.04834	0.00222	174.69	4.30	174.76	10.70	77.78	36.55	1.00	
9	0.02738	0.00066	0.18306	0.00877	0.04840	0.00244	174.10	4.15	170.31	7.55	67.63	36.64	1.02	
10	0.02787	0.00062	0.17619	0.01055	0.04620	0.00295	177.20	3.92	164.23	9.07	94.04	36.13	1.08	x
11	0.02797	0.00085	0.19640	0.00873	0.05101	0.00214	177.78	5.33	181.71	7.44	68.38	36.21	0.98	
12	0.02861	0.00076	0.19328	0.01128	0.05005	0.00269	181.81	4.78	178.82	9.59	97.17	35.29	1.02	
13	0.02892	0.00091	0.33271	0.04856	0.08064	0.01069	183.76	5.72	283.12	35.20	238.61	35.04	0.65	x
14	0.02875	0.00065	0.19276	0.00999	0.04846	0.00242	182.70	4.08	178.50	8.47	87.44	35.02	1.02	
15	0.02790	0.00072	0.19434	0.01148	0.04971	0.00279	177.38	4.49	179.70	9.71	92.74	36.17	0.99	
16	0.02759	0.00072	0.19363	0.01370	0.05095	0.00311	175.45	4.52	178.83	11.57	100.04	36.58	0.98	
17	0.02815	0.00095	0.20682	0.01743	0.05298	0.00349	178.91	5.94	189.47	14.53	115.40	36.09	0.94	
18	0.02819	0.00071	0.20454	0.01105	0.05200	0.00261	179.18	4.45	188.39	9.33	88.03	35.79	0.95	
19	0.02771	0.00079	0.19169	0.01153	0.05012	0.00274	176.15	4.97	177.43	9.79	88.70	36.28	0.99	
20	0.02794	0.00100	0.18917	0.01563	0.05059	0.00391	177.62	6.25	174.75	13.28	144.19	36.41	1.02	
21	0.02819	0.00095	0.27659	0.02124	0.07153	0.00542	179.16	5.98	246.03	16.83	142.95	35.80	0.73	x
22	0.02722	0.00075	0.19489	0.01159	0.05119	0.00309	173.13	4.69	180.14	9.80	99.33	37.11	0.96	
23	0.02813	0.00079	0.20419	0.01278	0.05444	0.00357	178.79	4.96	187.90	10.71	118.47	35.92	0.95	
24	0.02689	0.00089	0.19200	0.01349	0.05001	0.00329	171.04	5.57	177.46	11.51	104.34	37.78	0.96	
25	0.02817	0.00079	0.18646	0.01232	0.04902	0.00319	179.06	4.96	172.86	10.59	100.98	35.88	1.04	
26	0.02700	0.00072	0.19611	0.01168	0.05251	0.00341	171.70	4.55	181.18	9.89	107.76	37.39	0.95	
27	0.02797	0.00085	0.25541	0.01710	0.06538	0.00423	177.79	5.33	229.68	13.73	128.87	36.24	0.77	x
28	0.02797	0.00076	0.22635	0.00969	0.05799	0.00242	177.83	4.77	208.48	8.64	78.63	35.90	0.85	x
29	0.02700	0.00070	0.20166	0.01231	0.05559	0.00314	171.69	4.41	185.82	10.33	93.62	37.16	0.92	
30	0.02658	0.00059	0.17900	0.01228	0.04844	0.00319	169.12	3.70	166.46	10.51	119.56	37.72	1.02	
31	0.02822	0.00071	0.20609	0.01403	0.05300	0.00320	179.39	4.47	189.32	11.81	94.13	35.76	0.95	
32	0.02823	0.00094	0.27751	0.02378	0.07359	0.00639	179.41	5.87	246.30	18.71	163.10	35.67	0.73	x
33	0.02810	0.00081	0.20412	0.01202	0.05348	0.00323	178.63	5.06	187.92	10.15	92.37	35.99	0.95	
34	0.02473	0.00097	0.19730	0.01523	0.05872	0.00496	157.45	6.10	181.69	12.73	163.05	41.41	0.87	x
35	0.02990	0.00121	0.25620	0.02823	0.06202	0.00549	189.87	7.56	229.15	22.11	160.41	34.01	0.83	x
36	0.02790	0.00069	0.20193	0.01394	0.05264	0.00311	177.37	4.33	185.84	11.73	103.39	36.14	0.95	
37	0.02779	0.00079	0.20903	0.01542	0.05551	0.00366	176.70	4.96	191.80	12.78	122.05	36.31	0.92	
38	0.02766	0.00073	0.20344	0.01208	0.05216	0.00248	175.87	4.59	187.35	10.14	71.69	36.10	0.94	
39	0.02809	0.00089	0.24794	0.02920	0.06349	0.00736	178.53	5.58	221.31	23.01	205.97	36.09	0.81	x
40	0.02839	0.00070	0.20683	0.01256	0.05252	0.00281	180.46	4.38	190.14	10.59	82.82	35.33	0.95	
41	0.02755	0.00071	0.18862	0.01078	0.04986	0.00239	175.15	4.48	174.89	9.24	61.60	36.63	1.00	
42	0.02753	0.00088	0.18356	0.01536	0.04962	0.00401	175.07	5.55	169.95	13.09	129.39	36.59	1.03	
43	0.02606	0.00110	0.23794	0.02785	0.06502	0.00647	165.80	6.89	213.61	21.15	210.30	39.26	0.78	x
44	0.02713	0.00091	0.19679	0.01142	0.05188	0.00243	172.54	5.70	181.79	9.68	72.83	37.41	0.95	
45	0.02847	0.00096	0.18225	0.01074	0.04884	0.00243	180.92	6.03	169.42	9.27	72.78	35.69	1.07	x
46	0.02663	0.00081	0.21815	0.01810	0.05964	0.00455	169.37	5.10	194.63	11.64	126.91	38.03	0.87	x
47	0.02822	0.00096	0.19335	0.01184	0.04957	0.00314	179.34	6.03	178.81	10.04	98.14	36.01	1.00	
48	0.02762	0.00098	0.20445	0.01214	0.05530	0.00336	175.61	6.16	188.20	10.15	103.79	36.81	0.93	
49	0.02819	0.00075	0.19413	0.01143	0.05028	0.00273	179.19	4.72	179.50	9.70	90.48	35.66	1.00	
50	0.02777	0.00076	0.20434	0.01239	0.05356	0.00273	176.54	4.76	188.07	10.46	81.49	36.18	0.94	
51	0.02818	0.00076	0.18689	0.00825	0.04889	0.00230	179.14	4.78	173.64	7.02	89.11	35.63	1.03	
52	0.02812	0.00082	0.21813	0.01611	0.05652	0.00353	178.76	5.13	199.16	13.37	104.68	35.97	0.90	
53	0.02757	0.00096	0.20048	0.01110	0.05297	0.00278	175.30	6.00	187.00	10.12	89.21	36.84	0.94	
54	0.02747	0.00092	0.19054	0.01221	0.05104	0.00304	174.66	5.75	176.37	10.40	87.88	36.98	0.99	
55	0.02807	0.00095	0.20027	0.00786	0.05220	0.00233	178.44	5.97	185.06	6.67	80.90	36.17	0.96	
56	0.02805	0.00081	0.19469	0.01137	0.05035	0.00257	178.33	5.05	180.00	9.66	76.82	36.02	0.99	
57	0.02861	0.00088	0.23445	0.02282	0.05906	0.00482	181.79	5.48	211.65	18.00	163.10	35.39	0.86	x
58	0.02821	0.00089	0.20198	0.01190	0.05099	0.00289	179.31	5.57	186.13	10.01	90.91	35.67	0.96	
59	0.02756	0.00077	0.18914	0.00993	0.04949	0.00249	175.26	4.84	175.41	8.48	88.00	36.48	1.00	
60	0.02815	0.00068	0.19814	0.01045	0.05154	0.00260	178.93	4.24	183.03	8.80	77.84	35.64	0.98	
61	0.02775	0.00083	0.19915	0.01509	0.05178	0.00305	176.43	5.19	183.34	12.62	95.46	36.19	0.96	
62	0.02846	0.00082	0.18951	0.01082	0.04879	0.00257	180.86	5.16	175.63	9.21	89.37	35.55	1.03	
63	0.02813	0.00105	0.19458	0.01352	0.05072	0.00306	178.78	6.58	179.63	11.51	92.12	36.25	1.00	
64	0.02828	0.00081	0.19156	0.01216	0.05008	0.00274	179.76	5.07	177.24	10.38	84.65	35.75	1.01	

65	0.02851	0.00085	0.26970	0.02677	0.06991	0.00648	181.20	5.34	239.62	20.31	158.63	35.50	0.76	x
66	0.02818	0.00079	0.19973	0.01361	0.05210	0.00350	179.10	4.98	184.03	11.44	127.65	35.89	0.97	
67	0.02873	0.00137	0.28236	0.03996	0.07015	0.00804	182.55	8.57	248.96	30.07	206.46	35.45	0.73	x
68	0.02773	0.00067	0.18752	0.01010	0.04906	0.00262	176.28	4.19	174.01	8.61	91.07	35.98	1.01	
69	0.02759	0.00065	0.19009	0.01306	0.05003	0.00331	175.40	4.05	175.89	11.12	107.80	36.52	1.00	
70	0.02884	0.00095	0.20206	0.01136	0.05141	0.00294	183.26	5.94	186.26	9.57	93.68	35.16	0.98	
71	0.02717	0.00117	0.18024	0.01896	0.04781	0.00516	172.75	7.35	170.11	17.85	146.78	37.02	1.02	
72	0.02775	0.00094	0.17980	0.01297	0.04651	0.00358	176.39	5.90	167.07	11.15	130.03	36.62	1.06	x
73	0.02900	0.00122	0.24766	0.03926	0.06117	0.00822	184.26	7.64	218.65	29.27	273.56	34.97	0.84	x
74	0.02514	0.00122	0.34884	0.07664	0.10030	0.02011	159.99	7.67	285.01	49.86	312.13	41.12	0.56	x
75	0.02775	0.00104	0.19754	0.01209	0.05215	0.00306	176.40	6.51	182.35	10.21	101.47	36.13	0.97	
76	0.02825	0.00126	0.24128	0.01848	0.06072	0.00477	179.51	7.92	217.96	15.06	146.03	35.99	0.82	x
77	0.02663	0.00092	0.19746	0.01093	0.05308	0.00287	169.41	5.80	182.39	9.29	87.30	37.86	0.93	
78	0.02751	0.00099	0.18604	0.01257	0.04962	0.00299	174.93	6.23	172.48	10.75	97.56	36.69	1.01	
79	0.02761	0.00104	0.20411	0.01295	0.05422	0.00319	175.52	6.53	187.79	10.87	107.38	36.92	0.93	
80	0.02621	0.00073	0.18734	0.01504	0.04951	0.00258	166.79	4.62	173.37	12.84	69.76	38.53	0.96	
81	0.02779	0.00097	0.19175	0.01285	0.05112	0.00324	176.68	6.10	177.34	10.77	111.77	36.32	1.00	
82	0.02676	0.00120	0.27941	0.02514	0.07606	0.00635	170.15	7.52	247.64	19.42	153.57	38.46	0.69	x
83	0.02958	0.00084	0.43958	0.02976	0.11047	0.00688	187.89	5.28	367.03	21.00	119.87	34.18	0.51	x
84	0.02690	0.00137	0.34749	0.04406	0.09208	0.00976	171.03	8.61	297.14	32.09	161.78	38.17	0.58	x
85	0.02801	0.00097	0.20711	0.01269	0.05332	0.00343	178.02	6.10	190.37	10.68	106.95	36.29	0.94	
86	0.02661	0.00099	0.18846	0.01533	0.05006	0.00395	169.28	6.22	174.18	13.00	128.24	37.99	0.97	
87	0.02789	0.00071	0.20514	0.01096	0.05236	0.00255	177.31	4.48	188.90	9.25	73.37	36.17	0.94	
88	0.02620	0.00103	0.18188	0.01304	0.05172	0.00373	166.69	6.47	168.84	11.22	111.29	38.96	0.99	
89	0.02844	0.00111	0.19096	0.01350	0.04871	0.00284	180.72	6.94	176.58	11.57	95.55	35.29	1.02	
90	0.02760	0.00094	0.20185	0.01203	0.05322	0.00301	175.45	5.88	188.25	11.02	107.10	36.81	0.93	
91	0.02826	0.00065	0.20193	0.01053	0.05044	0.00206	179.64	4.06	186.22	8.86	65.97	35.65	0.96	
92	0.02727	0.00058	0.20242	0.00743	0.05376	0.00207	173.43	3.64	186.91	6.27	72.91	36.89	0.93	
93	0.02807	0.00042	0.19223	0.00854	0.05052	0.00213	178.44	2.66	178.18	7.25	75.76	35.74	1.00	
94	0.02933	0.00063	0.36871	0.05431	0.08725	0.01087	186.33	3.97	308.86	37.60	219.56	34.31	0.60	x
95	0.02797	0.00069	0.22045	0.01172	0.05647	0.00256	177.81	4.33	201.66	9.71	83.37	36.06	0.88	x
96	0.02827	0.00069	0.24494	0.01873	0.06098	0.00396	179.70	4.33	220.93	14.90	121.35	35.66	0.81	x
97	0.02830	0.00073	0.31331	0.01600	0.08039	0.00466	179.91	4.56	275.71	12.31	114.02	35.66	0.65	x
98	0.02805	0.00066	0.31087	0.02311	0.07933	0.00574	178.30	4.15	272.77	17.62	125.96	35.93	0.65	x
99	0.02709	0.00082	0.21791	0.01305	0.05884	0.00324	172.29	5.13	199.38	10.93	100.02	37.34	0.86	x
100	0.02740	0.00054	0.19605	0.01089	0.05176	0.00274	174.27	3.36	181.20	9.20	87.01	36.54	0.96	
101	0.02861	0.00045	0.19995	0.00866	0.05059	0.00188	181.84	2.84	184.72	7.30	64.22	34.95	0.98	
102	0.02835	0.00056	0.29030	0.02408	0.07513	0.00602	180.23	3.51	256.47	18.59	141.38	35.45	0.70	x
103	0.02889	0.00073	0.19789	0.01583	0.04876	0.00291	183.55	4.59	182.19	13.00	144.07	34.93	1.01	
104	0.02748	0.00058	0.20970	0.01075	0.05476	0.00270	174.71	3.62	192.76	8.99	87.04	36.44	0.91	
105	0.02713	0.00062	0.22448	0.01634	0.06053	0.00414	172.52	3.91	204.60	13.45	128.84	37.09	0.84	x
106	0.02820	0.00077	0.22457	0.01318	0.05911	0.00336	179.25	4.86	204.91	10.93	100.56	35.58	0.87	x
107	0.02750	0.00090	0.26160	0.01307	0.06834	0.00348	174.85	5.67	235.22	10.49	96.89	36.68	0.74	x
108	0.02800	0.00099	0.19623	0.01011	0.05104	0.00304	177.98	6.20	181.44	8.56	108.75	36.34	0.98	
109	0.02744	0.00112	0.23236	0.02029	0.05975	0.00399	174.46	7.02	210.30	16.64	113.55	36.94	0.83	x
110	0.02795	0.00083	0.19354	0.01228	0.05068	0.00307	177.65	5.19	178.93	10.40	100.37	36.20	0.99	
111	0.02840	0.00109	0.20241	0.01472	0.05296	0.00321	180.48	6.83	186.14	12.36	96.98	35.54	0.97	
112	0.02778	0.00104	0.18355	0.00982	0.04866	0.00243	176.56	6.51	172.49	9.11	87.80	36.70	1.02	
113	0.02737	0.00108	0.21326	0.00994	0.05671	0.00231	174.00	6.76	195.83	8.32	80.59	37.26	0.89	x
114	0.02767	0.00093	0.19244	0.01348	0.05030	0.00301	175.93	5.85	180.27	10.56	100.39	36.50	0.98	
115	0.02692	0.00117	0.18492	0.01516	0.04878	0.00358	171.18	7.32	171.17	13.00	94.31	37.71	1.00	
116	0.02741	0.00110	0.20044	0.01744	0.05123	0.00403	174.30	6.89	184.05	14.76	121.20	37.34	0.95	
117	0.02656	0.00114	0.20759	0.01526	0.05647	0.00371	168.95	7.16	190.45	12.67	113.62	38.57	0.89	x
118	0.02809	0.00097	0.20674	0.01531	0.05311	0.00355	178.56	6.07	189.72	12.78	117.07	36.19	0.94	
119	0.02731	0.00100	0.19668	0.01196	0.05205	0.00254	173.68	6.25	181.63	10.08	83.83	37.25	0.96	
120	0.02786	0.00096	0.21881	0.01588	0.05618	0.00410	178.48	6.56	199.76	13.22	120.71	36.27	0.89	x
121	0.02701	0.00107	0.22304	0.01917	0.06199	0.00458	171.76	6.71	202.80	15.61	136.24	37.81	0.85	x
122	0.02860	0.00120	0.20203	0.01325	0.05239	0.00376	181.71	7.49	186.01	11.14	123.23	35.41	0.98	
123	0.02786	0.00080	0.22712	0.01749	0.05715	0.00378	177.13	5.01	206.44	14.18	110.87	36.31	0.86	x
124	0.02786	0.00084	0.21206	0.01222	0.05535	0.00268	177.10	5.25	196.80	10.99	103.39	36.35	0.90	
125	0.03067	0.00148	0.70965	0.07531	0.16466	0.01375	194.64	9.28	532.35	41.96	146.58	33.19	0.37	x
126	0.02832	0.00132	0.25339	0.02459	0.06654	0.00606	179.97	8.25	226.77	19.47	159.53	36.02	0.79	x
127	0.02634	0.00095	0.30242	0.02451	0.08374	0.00586	167.57	5.96	265.91	18.82	153.84	38.62	0.63	x
128	0.02740	0.00111	0.31599	0.02133	0.08153	0.00518	174.21	6.94	277.00	16.55	119.48	37.07	0.63	x
129	0.02807	0.00095	0.20869	0.01161	0.05452	0.00241	178.39	5.96	191.82	9.76	76.13	35.87	0.93	
130	0.02746	0.00109	0.19578	0.01107	0.05200	0.00292	174.57	6.86	180.96	9.41	98.31	36.90	0.96	
131	0.02814	0.00095	0.28171	0.03553	0.07194	0.00829	178.84	5.96	252.72	28.41	202.24	35.82	0.71	x
132	0.02767	0.00091	0.26019	0.01687	0.06786	0.00388	175.94	5.73	233.61	13.43	104.30	36.67	0.75	x
133	0.02728	0.00082	0.24311	0.01490	0.06552	0.00355	173.45	5.14	219.99	12.06	103.91	37.10	0.79	x
134	0.02849	0.00124	0.23812	0.01847	0.06122	0.00405	181.00	7.75	215.37	15.07	122.16	35.37	0.84	x

135	0.02410	0.00103	0.22719	0.02321	0.06869	0.00583	153.46	6.50	205.52	18.89	148.52	42.05	0.75	x
136	0.03113	0.00111	0.58695	0.07390	0.13790	0.01433	197.55	6.94	464.61	48.57	175.87	32.66	0.43	x
137	0.02832	0.00088	0.27345	0.02236	0.06877	0.00585	179.98	5.49	247.12	19.00	156.11	35.78	0.73	x
138	0.02985	0.00134	0.26982	0.02150	0.06301	0.00402	189.57	8.36	240.62	16.95	122.80	34.39	0.79	x
139	0.02685	0.00095	0.27471	0.01932	0.07337	0.00427	170.79	5.97	244.86	15.27	105.23	37.90	0.70	x
140	0.02767	0.00135	0.21493	0.01766	0.05647	0.00422	175.85	8.43	196.25	14.62	125.55	36.91	0.90	
141	0.02885	0.00138	0.30113	0.02678	0.07634	0.00570	185.26	7.79	264.42	20.40	137.87	34.97	0.70	x
142	0.02805	0.00070	0.30506	0.01932	0.07904	0.00515	178.30	4.37	268.86	14.93	129.86	35.81	0.66	x
143	0.02881	0.00082	0.24881	0.01231	0.06288	0.00346	183.08	5.15	224.94	10.00	106.46	35.09	0.81	x
144	0.02708	0.00083	0.21225	0.01259	0.05668	0.00317	172.23	5.19	194.70	10.54	96.59	37.40	0.88	x
145	0.02832	0.00124	0.21036	0.01284	0.05260	0.00278	179.96	7.75	193.09	10.77	78.10	36.25	0.93	
146	0.02768	0.00101	0.22616	0.01195	0.05758	0.00294	175.99	6.36	206.38	9.87	97.31	36.61	0.85	x
147	0.02723	0.00110	0.28266	0.01788	0.07611	0.00451	173.13	6.91	251.45	13.97	120.40	36.95	0.69	x
148	0.02810	0.00111	0.23978	0.01524	0.06124	0.00343	178.59	6.96	217.22	12.39	106.50	36.37	0.82	x
149	0.02956	0.00081	0.28158	0.01548	0.06989	0.00385	187.76	5.07	250.91	12.26	105.92	34.18	0.75	x
150	0.02727	0.00109	0.26209	0.01597	0.06908	0.00388	173.36	6.84	235.25	12.90	99.38	37.24	0.74	x
151	0.02869	0.00125	0.21172	0.01179	0.05486	0.00301	182.31	7.84	194.35	9.84	88.73	35.75	0.94	
152	0.02723	0.00141	0.33562	0.02673	0.08783	0.00621	173.09	8.84	295.57	21.60	140.05	38.01	0.59	x
153	0.02937	0.00126	0.53715	0.06680	0.13506	0.01666	186.57	7.90	433.45	44.14	205.31	35.00	0.43	x
154	0.02778	0.00105	0.20988	0.02072	0.05219	0.00431	176.59	6.61	191.46	17.24	142.42	36.47	0.92	
155	0.02847	0.00089	0.27298	0.02822	0.07033	0.00677	180.92	5.59	241.78	22.12	171.09	35.36	0.75	x
156	0.02634	0.00120	0.20220	0.01725	0.05568	0.00384	167.54	7.53	188.75	15.59	106.09	38.96	0.89	x
157	0.02830	0.00118	0.30456	0.03252	0.08048	0.00900	179.86	7.42	265.67	25.12	187.25	36.16	0.68	x
158	0.02831	0.00107	0.18276	0.01123	0.04673	0.00259	179.92	6.69	169.82	9.63	83.73	35.69	1.06	x
159	0.02661	0.00099	0.20642	0.01280	0.05576	0.00327	169.24	6.24	189.78	10.69	114.05	38.30	0.89	x
160	0.02840	0.00083	0.21767	0.01400	0.05453	0.00333	180.50	5.21	199.07	11.64	119.66	35.41	0.91	

Notes: Excluded analyses (Ex. column) >10% normal discordance or >5% reverse discordance (Conc. column lists concordance).

GEOLOGIC MAP OF THE NORTHERN PINE NUT MOUTAINS, NEVADA

Michael C. Say and Andrew V. Zuza

Quaternary deposits

- Qx — Anthropogenic deposits
- Qa — Youngest active alluvium
- Qsa — Spring deposits, gypsum
- Qpl — Playa deposits
- Qfy — Young active fan alluvium
- Qao — Old inactive alluvium, colluvium, talus
- Qls — Landslide deposits
- Qfi — Intermediate fan alluvium, undivided
- Qfo — Old fan alluvium, undivided
- Qp — Pediment deposits, gravels on broad flat surfaces

Tertiary volcanic and sedimentary rocks

- Tvc4 — Volcaniclastic cobble conglomerate
- Tbay — Youngest apahnitic basaltic andesite
- Tba — Aphanitic basaltic andesite, related volcanic breccia, undivided
- Tds — Diatamaceous shale and siltstone
- Tvc3 — Dacite related volcaniclastic, silicified sediments, undivided
- Tad — Porphyritic dacite and andesite flows, related interbedded volcaniclastic, undivided
- Tdi — Intrusive porphyritic dacite
- Tai — Intrusive porphyritic andesite
- Tvc2 — White cobble volcaniclastic, breccia, reworked hornblende tuff
- Tac — Como andesite, aphanitic basaltic andesite flows, sparse interbedded volcanic breccia, undivided
- Tact — Interbedded reworked tuff, pebble to cobble volcaniclastic
- Tvc1 — Andesitic boulder to cobble volcaniclastic, sandstone, undivided
- Ta — Andesite flows, undivided
- Tvc — Volcaniclastic, undivided
- Tss — Gray to dark gray shale
- Tcb — Black lahar channels
- Tdo — Old porphyritic hornblende dacite
- Tbt — Biotite-hornblende ash flow tuff

Jurassic volcaniclastic and sedimentary rocks

- Jg — Gardnerville Formation, limestone and siltstone

Inclined volcanic flow foliation

Inclined bedding

U-Pb zircon sample

$^{40}Ar/^{39}Ar$ sample

Geochemistry sample

Normal Fault, showing dip and striation, ball on down thrown side
Dashed where approximate, dotted where concealed, queried if identity or existence unknown

Strike-Slip Fault, showing dip and striation, arrows show relative motion
Dashed where approximate, dotted where concealed, queried if identity or existence unknown

Contact
Dashed where approximate, dotted where concealed

Scale 1:24,000
Contour Interval 40 Feet

1 .5 0 1 2 3 4 5 Kilometers

Projection: Universal Transverse Mercator, Zone 11, North American Datum 1983

APPROXIMATE MEAN DECLINATION, 2019

Map Location

Adjoining 7.5' Quadrangle Names

1. Flowery Peak
2. Moffits Flat
3. Churchill Butte
4. Como
5. Como
6. Churchill Canyon Well

Base Map: U.S. Geological Survey Flowery Peak 7.5' quadrangle (2018)
Base Map: U.S. Geological Survey Moffits Flat 7.5' quadrangle (2018)
Base Map: U.S. Geological Survey Churchill Butte 7.5' quadrangle (2018)
Base Map: U.S. Geological Survey Como 7.5' quadrangle (2018)
Base Map: U.S. Geological Survey Como 7.5' quadrangle (2018)
Base Map: U.S. Geological Survey Churchill Canyon Well 7.5' quadrangle (2018)

Sources of Existing Mapping

1. Stewart (1999)
2. Vikre and McKee (1994)
3. Russell (1981)

A8